AIAA Journal Accepted Manuscript Sept. 15, 2016. Published (Vol. 55, No. 4, 2017) by the American Institute of Aeronautics and Astronautics, Inc. with permission. DOI 10.2514/1.J055144

State-Space Adaptation of Unsteady Lifting Line Theory: Twisting/Flapping Wings of Finite-Span

Jacob S. Izraelevitz *
Massachusetts Institute of Technology, Cambridge, MA 02139

Qiang Zhu†
UC San Diego, San Diego, CA 92093

Michael S. Triantafyllou ‡
Massachusetts Institute of Technology, Cambridge, MA 02139

We analytically derive a low order state-space adaptation of the unsteady lifting line model for a wing of finite aspect-ratio, suitable for use in real-time control of wake-dependent forces. Each discretization along the span has from 1 to 6 states to represent the local unsteady wake effects, rather than remembering the entire wake history which unnecessarily complicates controller design. Sinusoidal perturbations to each system degree-of-freedom are also avoided. Instead, a state-space model is fit to individual indicial functions for each blade element, allowing the downwash and lift distributions over the span to be arbitrary. The wake geometry is assumed to be quasi-steady (no rollup) but with fully unsteady vorticity. The model supports time-varying surge (a nonlinear effect), dihedral, heave, sweep, and twist along the span. Cross-coupling terms are explicitly derived. We then validate this state-space model through comparison with an analytic solution for elliptic wings, an unsteady vortex lattice method, and experiments from the literature.

Nomenclature

A_ϕ, A_Γ, A_w	=	amplitude of exponential in $\phi(\tilde{t})$, $\tilde{\Gamma}(\tilde{t})$, or $w_{\Gamma,2D}(\tilde{t})$
$\mathcal{AR}$	=	aspect ratio $\mathcal{AR} = b^2/S$
b_ϕ, b_Γ, b_w	=	exponent in approximation to $\phi(\tilde{t})$, $\tilde{\Gamma}(\tilde{t})$, or $w_{\Gamma,2D}(\tilde{t})$
b	=	wing span [m]
c^i	=	chord [m], measured perpendicular to wing sweep
i, j	=	indices of blade elements along span
k_{mid}	=	reduced frequency of mid-span $k_{\text{mid}} = \omega c_{\text{mid}}/2U$
L^i	=	section lift [N/m]
n	=	number of blade elements
N	=	total number of states $N = nN_\Gamma + nN_\phi + nN_w$
N_ϕ, N_Γ, N_w	=	lift, circulation, and downwash states per element
S	=	wing area [m^2]
t	=	time [s]
$\tilde{t}$	=	travel distance in half-chords
T	=	oscillation period [s]
U	=	steady wing velocity [m/s]
$v_n^i, v_\perp^i, v_s^i$	=	wing velocity components [m/s] evaluated at ¾-chord
v_e^i	=	wing effective normalwash [m/s] ($v_e = v_n + w_n$)
$w_n^i, \boldsymbol{w}_n$	=	wing downwash [m/s], as in lifting line theory
W_n	=	aerodynamic influence matrix [1/m], normal to wing
W_0, W_1, W_2	=	wake correction cross-coupling matrices
$w_{\Gamma,2D}$	=	downwash for step increase in 2D circulation [1/m]
$x_\phi^i, x_\Gamma^i, x_w^i$	=	lift, circulation, and downwash states [m/s]
$\alpha_{\max}$	=	maximum angle of attack at pitching axis
$\Gamma^i, \boldsymbol{\Gamma}$	=	circulation [m^2/s] of blade section i
$\tilde{\Gamma}(\tilde{t})$	=	normalized circulation step response
Δs	=	blade section width [m]
λ	=	normalized velocity surge amplitude
ρ	=	fluid density [kg/m^3]
$\phi(\tilde{t})$	=	Wagner function, normalized lift step response
ω	=	oscillation frequency [rad/s]

*Ph.D. Candidate, Dept. of Mechanical Engineering jsi@mit.edu
†Associate Professor, Dept. of Structural Engineering qizhu@ucsd.edu
‡Professor, Dept. of Mechanical Engineering mistetri@mit.edu

I. Introduction

A. Motivation

Super-maneuverablity, expertly performed by many natural fliers, is an increasingly desirable design goal due to growing popularity of unmanned aerial vehicles [1]. Such vehicles call for maneuvering capabilities well within their own length scales, creating strong wake-induced effects that must be included in control design. Examples include active flutter suppression, avoidance of densely-packed obstacles, evasive maneuvers, or simply tracking aggressive trajectories.

Flapping-wing propulsion appears to be exquisitely adapted to providing such flight control [2]. The entirety of the wing can act as a propulsion apparatus, an aileron, or a lifting surface. Biological wings are often highly deformable, jointed, dynamic structures [3]. A bird wing achieves over 7 degrees-of-freedom control [4] via 45 muscles [5], in addition to the passive dynamics due to its structural flexibility. Moreover, evidence also shows that birds actively control their wing trajectories to compensate for changes in the environment [4].

The control of such complicated wings is inevitably nonlinear and difficult. A critical step is to predict the unsteady forces. However, for a prediction method to be useful for real-time control, the system information must be compacted into a small number of states. Otherwise, developing the control law becomes computationally intractable. Most optimal nonlinear control algorithms suffer from Bellman's "Curse of Dimensionality" [6] to explore the state space, and have runtimes that scale *exponentially* with the number of states.

Therefore, while full computational fluid dynamics simulations (millions of states) are physically accurate, they are infeasible in control purposes. Alternatively, an unsteady vortex lattice method (UVLM) on a modern computer is substantially faster, but still require far too many states (thousands), given that the full wake history must be recorded as individual vortex loops, and each loop constitutes a state - a "delay differential equation".

Fortunately, simulation *outputs* such as lift, downwash, and circulation appear to be easily represented by only tens of states. State space methods have been thereby successful in the control of unsteady aerodynamic phenomena, historically for the suppression of flutter [7]. A tremendous body of work in the flutter literature has fit linear, low-dimensional state-space models to sinusoidal perturbations to UVLM codes; for a thorough review, we refer the reader to [8]. Analytic solu-

tions have also been derived [9, 10] which can readily be adapted from frequency space into state-space for use in modern control frameworks. Reduced order modeling illustrates that while the true dynamics of unsteady wings are highly complicated, the outputs need not be.

Flapping flight modeling, while sharing a similar history to flutter, differs in a number of important aspects [11].

- Wing velocity is generally not constant, as natural fliers often move their wings fore-aft in addition to transverse to the flow [12].
- Wing heave is generally large amplitude compared to the chord, meaning that a linear analysis about a trim condition is not sufficient [13].
- Wing flapping frequencies are generally faster than the timescale of stall dynamics [14], lowering the importance of trailing edge stall modeling (with the exception of soaring flight), but increasing the importance of added mass terms and leading-edge vortex (LEV) shedding.

In this work, we analytically derive and validate a low-order state-space model that can be applied for use in the active control of flapping wings of finite span. Added mass terms are included, but LEV shedding is not. Analytic solutions to LEV modeling are still an active research topic [15], and prior work in [2] illustrates that LEV shedding can be controlled with an adequately robust control design. However, recent work in [16] has seen some success in representing LEVs with only a few states. Additionally, we also neglect trailing edge separation (distinct from trailing edge vortex shedding) given the high flapping frequencies, but this effect can certainly be modeled with additional states [17].

The most analogous work to this manuscript are Taha et. al. [18] and Peters et. al. [19], who also derive state-space models for unsteady 3D wings. However, Taha et. al. assumes a lift distribution a-priori in order to correct each blade element's unsteady behavior for the finite aspect-ratio. As noted by [10], the wing loading for an elliptic planform is far from elliptical in the unsteady case, so the finite aspect-ratio effects are not necessarily known. Dynamic wing loading is especially pronounced for the root-flapping motions of flapping flight, but can yet still be easily represented in state-space using our model.

Peters et. al. [19] also derive a state-space model for finite aspect-ratio wings, including an arbitrary lift distribution, but unfortunately limit the analysis to helicopter rotors of an assumed flat rotor plane. However, Peters's use of continuous spatial and temporal basis functions for representing the wake is analogous to the method outlined in this manuscript. Instead, we use a superposition of horseshoe vortices and 2D unsteady blade-element theory to represent the full 3D wake.

Our model contributes a key element that is lacking in prior work: we allow for a *fully dynamic wing circulation* over the lifting line using a small number of states (ranging from one to six) per blade element. Our model does not require recording the full wake history and does not need to be calibrated by additional simulations to provide reasonable predictions. Given the large state deviations from any linearizable steady state, linearization has been avoided whenever possible, although we do make a large assumption about the local flatness of the wake near the wing.

B. State-Space Method Overview

The wake of a flapping wing, ignoring viscous effects and LEV shedding, is usually modeled as a continuous vortex sheet. This wake accounts for both changes in wing circulation along the span (trailers), and changes in circulation over time (starting/stopping vortices). Our proposed state-space model approximates the wake (Fig. 1a) as the sum of two parts:

- Horseshoe vortices of infinite length located along the wing's lifting line, with trailers tilted tangent to the instantaneous velocity of the originating vortex point.
- State-space systems that track the unsteady circulation and lift for each blade element, as if it were an infinite span wing. The integral effect of the wake is therefore recorded, instead of the full time history.

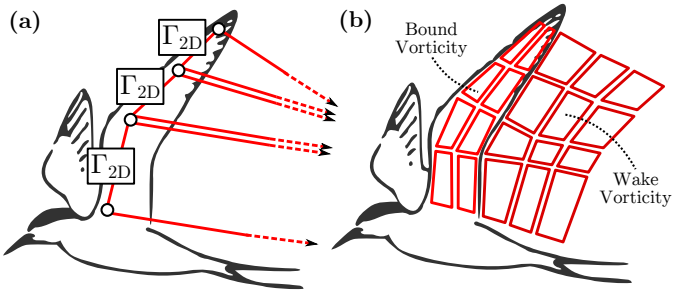

Figure 1. ***Wake Approximation*** **- Left (a): State-space formulation, each wing segment includes a 2D wing model along the lifting line, with inflow modified by the vortex trailers. Right (b): Unsteady vortex lattice theory for swept wings, discretized into vortex loops of constant circulation on both the wing and wake. Animal art modified from public domain content at https://openclipart.org.**

The wake model is therefore a combination of a fully unsteady 2D wake (state-space models), and a quasi-steady 3D wake (trailers) that couples each 2D wake to its neighbor. An additional small correction, described in Section II.D can further improve the accuracy of this rendition by deriving a full 3D coupling as expected from unsteady lifting line theory.

Our insertion of an unsteady 2D wake into the 3D lifting line approximation is based off the work of Jones [20], who performs a similar analysis to determine the step response of elliptic planform wings. Jones, however, assumes a circulation distribution a-priori to facilitate an analytic solution, a problem which we mitigate using discrete horseshoe vortices. *

An overview of the model is therefore as follows. On each evaluation at time t, four steps are taken in sequence:

1. The circulation is determined by solving the influence of both the trailers *and* the circulation states that represent the unsteady wake.
2. The instantaneous downwash is determined from the now known circulation, thereby modifying the incident velocity.
3. The lift is determined from the downwash and lift states.
4. The time-derivatives of all states are determined, then integrated in time to give the new states.

As is standard with state-space models, there is always a trade-off between the number of states, i.e. computational complexity, and accuracy of representing the response. To study the sensitivity of our model to the number of states, two different cases are considered: a six-state per wing segment (blade element) that almost exactly mimics the output of an unsteady vortex lattice solution, and a one-state per blade element model that is more suitable for early controller design. We then validate this model against an unsteady vortex lattice method (UVLM) code developed by Zhu et. al. [23], and experimental results from Scherer [24].

C. Validation Method Overview - Unsteady Vortex Lattice Method

Given that our state-space model is inviscid, UVLM (Fig. 1b) is a natural validation choice for verifying the model. UVLM has long been

*Despite this change, and unknown to Jones [20], the formulated unsteady lifting line model is not strictly consistent due to conflicting lengthscales. It attempts to represent a wake that has a wavelength λ_{wake} on the order of a few chordlengths ($\lambda_{wake} \approx c$), but only calculate the finite-span downwash on a single line ($\lambda_{wake} \gg c$). A rigorous investigation using matched asymptotic expansions of this issue can be found in [21, 22]. Nevertheless, the unsteady lifting line model works satisfactorily given that the 3D unsteady wake features, in contrast to each blade's 2D wake, are typically large enough scale to not promote induced flows that vary substantially over the chord.

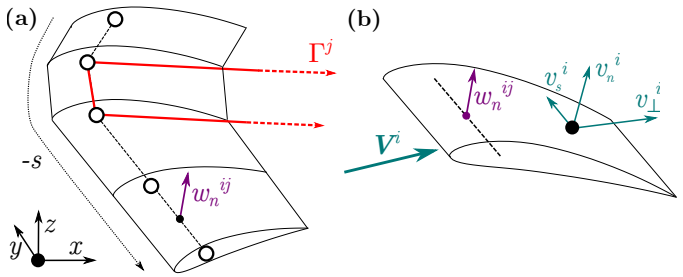

Figure 2. ***Component Velocities*** **- Left (a): Origin is fixed in the global frame, with aircraft moving to the left. Wing sections are indexed i from the left wingtip, and horseshoe vortices are indexed j from the left wingtip. Downwash w_n^{ij} is summed over all horseshoe vortices Γ^j. Right (b): Wing section velocity at ¾-chord point is decomposed in components normal, along sweep, and perpendicular to sweep.**

used for the study of flapping flight [25, 26, 27, 28] and is discussed in-depth in Katz and Plotkin's textbook [29]. This method acts as an almost exact comparison to our state-space model as it captures the same physics with only the extra inclusion of lifting surface effects. Our selected code, Zhu et. al. [23], has been successfully used in prior work for the study of fish swimming.

In UVLM, the flow potential is separated into two parts, one attributed to the influence of the body and the other to the influence of the wake. Hereby the wake is represented by a zero-thickness sheet with a distribution of dipole panels in it. Constant boundary elements are applied on both the body surface and the wake sheet, with each element equivalent to a vortex ring, automatically satisfying Kelvin's theorem on the conservation of circulation and zero flow divergence [29]. At every time step, new wake panels are shed from the sharp trailing edge. The strength of the newly shed panels is determined through the Kutta condition. Meanwhile the previously shed panels convect downstream following the incoming flow (and the induced velocity from the body and the wake itself; this induced velocity, however, is found to have negligible effect on the results of the problems we study). Once generated, the strength of the wake elements remains unchanged due to the lack of dissipation. Detailed description of this model is included in Zhu et. al. [23].

Therefore, the differences between the state-space model and UVLM can be attributed to lifting surface effects and a fuller wake representation. Neither method includes LEV's or trailing edge separation.

II. Model for Arbitrary 3D Motion

We derive our state-space model using the indicial method, applied to each blade section and then coupled using lifting line theory. Relevant reference frames and velocities are presented in Section II.A. Next, Section II.B enumerates the exponential approximations to the dynamics required to develop a state-space model. The states themselves, and their dynamics, are derived in Section II.C to give the scalar lift and circulation.

Subsequently, we propose modifications to the derived state-space model. Section II.D derives a small correction factor to consolidate the assumed wake structure. A simplified model, with fewer states, is given in Section II.E.

Finally, Section II.F calculates the vectorial lift, drag, and added mass forces from the scalar state values.

A. Reference Frames and Wake Discretization

First, we divide the wing into n blade elements. According to the modern numerical lifting line theory of swept wings [30], each element consists of a control point and a horseshoe vortex at ¼-chord (Fig. 2a). These elements are indexed $i = 1 \dots n$ from left to right wingtip. The legs of each horseshoe vortex lie coincident with their neighbor's legs, thereby creating vortex filaments of strength equal to the difference in circulation between blade elements. We do *not* discretize the wake in the streamwise direction (or in time), as in UVLM. Instead, the state-space model accounts for the unsteady wake effects of each blade.

Each leg of the horseshoe vortices are tilted to lie tangent to the local direction of oncoming flow. We then sum the induced velocities from all the horseshoe vortices to each control point as the downwash $\boldsymbol{w}$ [29]:

$$\boldsymbol{w}^{ij} = -\frac{\Gamma^j}{4\pi\|\boldsymbol{r}_L^{ij}\|}\frac{\hat{\boldsymbol{v}}_L^j \times \boldsymbol{r}_L^{ij}}{\|\boldsymbol{r}_L^{ij}\| - \hat{\boldsymbol{v}}_L^j \cdot \boldsymbol{r}_L^{ij}} + \frac{\Gamma^j}{4\pi\|\boldsymbol{r}_R^{ij}\|}\frac{\hat{\boldsymbol{v}}_R^j \times \boldsymbol{r}_R^{ij}}{\|\boldsymbol{r}_R^{ij}\| - \hat{\boldsymbol{v}}_R^j \cdot \boldsymbol{r}_R^{ij}}, \tag{1}$$

where $\hat{\boldsymbol{v}}_L^j$ and $\hat{\boldsymbol{v}}_R^j$ are the instantaneous velocity directions at the left and right trailer origin respectively, and $\boldsymbol{r}_L^{ij}$ and $\boldsymbol{r}_R^{ij}$ are the displacements of the control point i to trailer j. We now turn Eq. (1) into an aerodynamic influence matrix equation along the foil normal $\hat{\boldsymbol{n}}^i$, where matrix W_n is given element by element as $(\boldsymbol{w}^{ij} \cdot \hat{\boldsymbol{n}}^i)/\Gamma^j$:

$$\boldsymbol{w}_n = W_n \boldsymbol{\Gamma}. \tag{2}$$

Here, the vector notation is used to indicate a list of values, i.e. $\boldsymbol{w}_n = [w_n^{i=1}, w_n^{i=2} \dots]$, $\boldsymbol{\Gamma} = [\Gamma^{i=1}, \Gamma^{i=2} \dots]$ rather than a spatial vector. We continue this notation throughout the paper: a vector without an index, such as $\boldsymbol{u}$, can be considered a list of scalar values to ease matrix operations, while one with an index $\boldsymbol{u}^i$ is a spatial vector located at blade section i. Additionally, $\hat{\boldsymbol{u}}^i$ is the unit vector in the direction of $\boldsymbol{u}^i$.

In a swept wing, only the velocity perpendicular to the wing sweep affects the lift, so the free-stream must be modified accordingly [31]. On each blade element, we therefore decompose the time-varying flow velocity $\boldsymbol{V}^i(t)$, defined as equal and opposite to the body velocity, into three components in the body frame: $v_n(t)$, $v_\perp(t)$, and $v_s(t)$ (Fig. 2b).

Using the notation from [32], the velocity $v_n(t)$ is the component normal to the foil camberline, $v_s(t)$ is the component parallel to the wing sweep, and $v_\perp(t)$ is the magnitude of the velocity in the plane perpendicular to the sweep:

$$v_\perp^i = ||\boldsymbol{V}^i - \hat{\boldsymbol{s}}^i(\boldsymbol{V}^i \cdot \hat{\boldsymbol{s}}^i)||, \tag{3}$$

where $\hat{\boldsymbol{s}}^i$ is the direction following the wingsweep. Velocities $v_\perp(t)$ and $v_n(t)$ are not necessarily perpendicular, as $v_\perp(t)$ can include a component in the normal direction.

The origin of this body system is located at the wing section's ¾-chord point, as consistent with the unsteady 2D theory of Theodorsen [33] to include the lift proportional to pitch-rate and camber. For example, given a 2D wing with a distance r between the pitching axis and the ¾-chord point, the pitch rate $\dot{\theta}$, angle of attack α at the pitching axis, and no-lift angle of attack α_0, the normalwash is given by:

$$\text{2D Case: } v_n = V(\alpha_{3/4} - \alpha_0) = V(\alpha - \alpha_0) + \dot{\theta} r. \tag{4}$$

For pitching about the quarter-chord, $r = c/2$.

Note that though the relevant unsteady velocities are taken about ¾-chord point, we choose the wake downwash control point to be applied at the ¼-chord point and ignore the flow induced by the bound leg, as consistent with lifting line theory. Alternatively, one could move the control point to the ¾-chord point and include the bound leg, such as in Weissinger extended lifting line [34], but this will both underpredict the analytic solutions to the Prandlt lifting line problem [35] and lead to possible singularities if the horseshoe legs intersect the control points.

B. Indicial Functions of 2D Airfoil

We will employ the indicial method, similar to the one used by Jones [20], to derive the state-space representation of the system. In this approach, the step response of a 2D airfoil, and exponential approximations to that response, are critical to the success of the method.

First, we normalize the lift and circulation of the 2D airfoil step response by their steady-state values. The normalized lift step response is notated as the Wagner function $\phi(\tilde{t})$ [36]. The normalized circulation response is notated as $\tilde{\Gamma}(\tilde{t})$, equivalent to $\Gamma_0/2\pi$ in Jones's [20] notation. The exact values of $\tilde{\Gamma}(\tilde{t})$ and $\phi(\tilde{t})$ can be derived numerically by solving the 2D unsteady vortex lattice problem, i.e. enforcing the

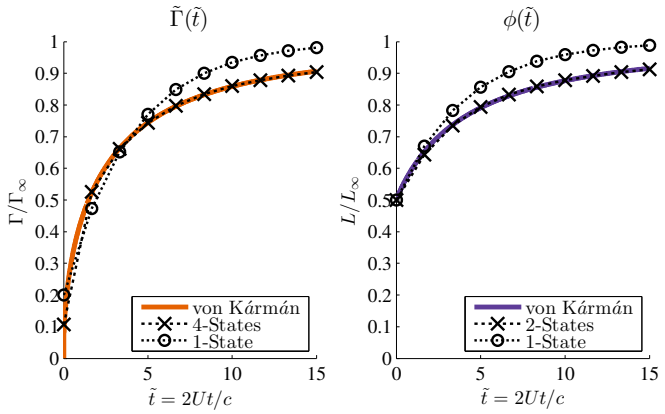

Figure 3. ***Indicial Functions*** **- Normalized lift $\phi(\tilde{t})$ and circulation $\tilde{\Gamma}(\tilde{t})$ for a step increase in 2D flat plate angle of attack, as dependent on distance traveled $\tilde{t}$. Exponential approximations of 1 to 4 poles are given in Table 1 to derive the state-space system.**

Kutta condition, conservation of circulation, and body boundary conditions on an airfoil with discrete wake vortices.

Von Kármán [37] compactly summarizes this problem with a set of differential-integral equations:

$$\tilde{\Gamma}(\tilde{t}) = \frac{\Gamma(\tilde{t})}{\Gamma(\infty)} = 1 - \int_0^{\tilde{t}} \left(\sqrt{\frac{\tilde{t}-\tau+2}{\tilde{t}-\tau}} - 1 \right) \dot{\tilde{\Gamma}}(\tau) d\tau, \tag{5}$$

$$\phi(\tilde{t}) = \frac{L(\tilde{t})}{L(\infty)} = 1 - \int_0^{\tilde{t}} \frac{\dot{\tilde{\Gamma}}(\tau) d\tau}{\sqrt{(\tilde{t}-\tau+1)^2 - 1}}, \tag{6}$$

where $L(\infty)$ is the steady-state lift force, and $\Gamma(\infty)$ is the steady-state airfoil circulation. Hereby $\tilde{t}$ is the dimensionless time, which coincides with the travel distance normalized by half the chord:

$$\tilde{t} = \frac{2}{c} \int_0^t v_\perp(\tau) d\tau. \tag{7}$$

In our notation, we use $\tilde{t}$ instead of the standard s for non-dimensional time to avoid confusion with either the Laplace variable or the spanwise coordinate. The body velocity $v_\perp$ can be time-varying.

Next, we approximate the step response using a sum of exponentials, which allows the model to be reduced to state-space representation. The lift $\phi(\tilde{t})$ is given as:

$$\phi(\tilde{t}) \approx 1 + A_{\phi 1} e^{b_{\phi 1} \tilde{t}} + A_{\phi 2} e^{b_{\phi 2} \tilde{t}} + ... \tag{8}$$

The circulation is approximated in a similar fashion:

$$\tilde{\Gamma}(\tilde{t}) \approx 1 + A_{\Gamma 1} e^{b_{\Gamma 1} \tilde{t}} + A_{\Gamma 2} e^{b_{\Gamma 2} \tilde{t}} + ... \tag{9}$$

Note that the lift and circulation are represented using different indicial functions. While the lift and circulation of an airfoil are proportional to each other in steady state, there is no such simple relation in the unsteady case. Using the Wagner function $\phi(\tilde{t})$ for circulation will actually over-predict the circulation at high reduced frequency. However, Lomax [9] gives an approximate expression for the relation between lift and circulation for $\tilde{t} > 8$:

$$\phi(\tilde{t}) \approx \tilde{\Gamma}(\tilde{t}) + \frac{3}{2} \frac{d\tilde{\Gamma}}{d\tilde{t}} \quad \text{for} \quad \tilde{t} > 8. \tag{10}$$

Equation (10) implies that for the slower poles, we can approximate $b_\Gamma \approx b_\phi$ and $A_\Gamma \approx A_\phi / [\frac{3}{2} b_\phi + 1]$. Reusing the same exponential b for both lift and circulation allows the same state to be shared between both quantities, thereby simplifying the dynamics and reducing the total number of states (see Section II.C). Furthermore, there is an additional benefit to sharing lift and circulation states: if the two quantities were kept artificially independent with nearly identical poles, the state-space representation on each blade would no longer be minimal, and would therefore contain an uncontrollable system mode.

Many exponential approximations of $\phi(\tilde{t})$ and $\tilde{\Gamma}(\tilde{t})$ exist, depending on the tradeoff between number of states and accuracy of the response. Approximations can additionally be determined from experimental data [38] or corrected for airfoil thickness effects [39]. Jones [20], in addition to approximations for $\phi(\tilde{t})$, also includes an approximation to $\tilde{\Gamma}(\tilde{t})$ that unfortunately does not converge to the steady state solution [40].

$\phi(\tilde{t})$	N_ϕ	A_ϕ	b_ϕ
Jones [20]	2	$[-0.165, -0.335]$	$[-0.045, -0.300]$
Drela [32]	1	-0.5	-0.25
$\tilde{\Gamma}(\tilde{t})$	N_Γ	A_Γ	b_Γ
Current Method	4	$[-0.177, -0.609, 0.170, -0.259]$	$[-0.045, -0.300, -0.433, -1.419]$
Current Method	1	-0.8	-0.25

Table 1. Exponential Approximations to Indicial Functions

In this particular study, we compare the following two approximations for $\phi(\tilde{t})$ (Fig. 3) with constants enumerated in Table 1:

- For an $N_\phi = 2$ states per blade element, we use Jones's [20] well known traditional values.
- For an $N_\phi = 1$ approximation, we use the values given by Drela [32], which exactly match the initial value, initial slope, and final asymptote of the true function.

Similarly, we also compare two approximations for $\tilde{\Gamma}(\tilde{t})$:

- For an $N_\Gamma = 4$ approximation, we reuse the $N_\phi = 2$ states using Lomax [9] Eq. (10). Two additional states (fit using Matlab's system identification toolbox) then compensate the high-frequency error between Eq. (10) and Eq. (5).
- For an $N_\Gamma = 1$ approximation, we reuse the $N_\phi = 1$ states again using Lomax [9] Eq. (10), and ignore higher frequency behavior.

C. State-Space Representation

By discretizing along the span, each section has independent circulation and lift. These two quantities are simulated using low-order state-space subsystems. Accordingly, rather than recording the full wake history (i.e. in UVLM), we only track several integral quantities as flow states and their rates of change, similar to [41, 17].

For the purposes of explaining the model, we will begin by employing the $N_\phi = 2$ and $N_\Gamma = 4$ state space approximations (Table 1). Therefore, at each location i along the span, the following states track the flow dynamics:

- Two states $x^i_{\phi 1}$ and $x^i_{\phi 2}$ represent the lift response of each blade element, as a function of the instantaneous normalwash $v^i_n(t)$ of the element and the downwash from all elements (and their wakes).
- Additionally, four states $x^i_{\Gamma 1}$, $x^i_{\Gamma 2}$, $x^i_{\Gamma 3}$, and $x^i_{\Gamma 4}$ represent the circulation Γ^i at each element. However, $x^i_{\phi 1}$ and $x^i_{\phi 2}$ have the same eigenvalues and inputs as the lower frequency circulation states $x^i_{\Gamma 1}$, $x^i_{\Gamma 2}$, allowing re-use of the lift states.

1. *Lift*

Following the standard Prandtl lifting line assumptions [35], we modify the normalwash $v_n(t)$ on each section with induced velocity $w_n(t)$

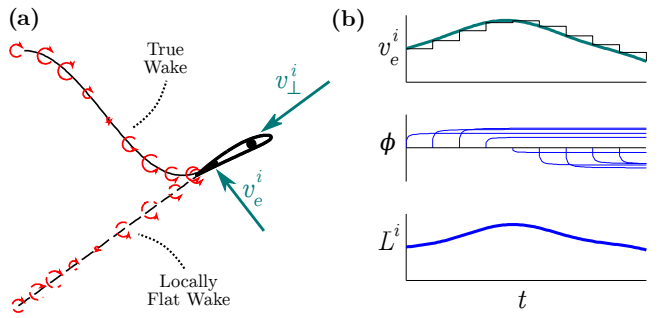

Figure 4. ***Duhamel Integral along Locally Flat Wake*** **- Left (a): Far wake is rotated to lie along tangent to instantaneous motion $v_\perp^i(t)$, thereby neglecting the 2D unsteady wake directional information. A Duhamel integral is then applied along the tilted flat wake. Right (b): Duhamel integral superposes differential variations in the effective normalwash v_e^i, which includes the downwash from all trailers. Each variation in v_e^i is multiplied by the Wagner function ϕ, then summed to give the section circulatory lift. A second step response $\tilde{\Gamma}$ is similarly integrated for the unsteady circulation.**

from the 3D trailing wake. Note that the downwash $w_n(t)$ is generally negative:

$$v_e^i(t) = v_n^i(t) + w_n^i(t). \tag{11}$$

Next, we briefly note the standard quasi-steady solution for lift of each blade section as [31]:

$$L_{\text{qs}}^i = \frac{1}{2}\rho c^i C_{l\alpha} v_\perp^i(t) v_e^i(t). \tag{12}$$

In this formulation, the lift force is proportional to the streamwise and normal velocity components of the body velocity, $v_\perp$ and v_e. Using $v_e = v_n + w_n$ instead of v_n accounts for 3D downwash, and $v_\perp(t)$ instead of $||V(t)||$ accounts for wing sweep.

A Duhamel integral allows us to determine the lift for arbitrary motions by superimposing the step response $\phi(\tilde{t})$ for differential variations in the effective foil normalwash v_e^i. The lift and circulation at each blade element therefore follow the unsteady 2D theory as developed by Wagner [36] and Theodorsen [33] for predicting the unsteady response due to a time-changing normalwash $v_n(t)$. Based on the results from Leishman and Beddoes [17], Hansen et al. [41] further suggest that this Duhamel integral can be represented in state-space, even if the wing velocity is time-varying.

Unfortunately, the standard Duhamel superposition approach assumes that the wake history effects are *only* dependent on the distance traveled from the time that wake was shed, meaning $\phi(\tilde{t})$ is the same for any foil trajectory. This is not the case for large heave or pitch oscillations, and technically only true for a flat wake located exactly downstream the airfoil (direction of U). However, given that the downwash due to each wake element dies as distance squared, the wake effects are generally dominated by the near-wake. Consequently, as postulated by Scherer [24], while wake superposition is technically inconsistent for an non-flat wake geometry, an accurate geometry of the local wake will reconstruct most of the unsteady 2D effects.

Therefore, in order to take advantage of superposition, we simplify the wake physics. We assume that the unsteady wake lies along the instantaneous motion vector of the blade element ¾-chord $v_\perp^i(t)$, computed from both the free-stream flow and the wing heave/surge/pitch (Fig. 4a), and follows a known decay rate with distance.

In other words, the wake is allowed to be unsteady, but with fixed geometry and dynamics given from the kinematics (locally flat wake geometry). Directional information of the far wake induced velocity is thereby lost, as all vortices induce a flow along the same direction. However, the induced flow can be at an angle to the free-stream, allowing the lift and downwash to tilt vectorially. The reference frame remains global, retaining the conservation of circulation.

Scherer [24] uses a similar assumption, though assumes the wake to lie tangent to the motion at ¼-chord; in reality, the difference between such details is small for realistic angles of attack and the lifting line approximation.

This assumption works surprisingly well, as validated in Section III, even for large wake curvature. Both lift and bound circulation of the wing are accurately predicted by the locally flat wake, for the tested range of normalized rotation rates up to $\dot{\theta}_{\max} c_{\text{mid}}/(2U) = 0.31$ in the heave/pitch oscillations of Section III.D. The obvious exception is wake-capture [42], where the wing intersects its own wake on subsequent flapping cycles. Wake-capture, while important for hovering flight of insects, cannot be modeled using this superposition and even requires special treatment in UVLM to avoid singularities.

Using the locally flat wake assumption, we can now superimpose an infinite number of step responses to reconstruct $L^i(t)$ from $v_e^i(t)$ as a Duhamel integral (Fig. 4b). Each step response is scaled by the change in v_e at that instant, and the decay of $\phi(\tilde{t})$ afterwards:

$$\frac{L^i(t)}{L_{\text{qs}}^i(t)} = \frac{1}{v_e^i(t)}\left[\phi(\tilde{t}) v_e^i(0) + \int_0^{\tilde{t}(t)} \phi(\tilde{t}-\sigma)\frac{dv_e^i(\sigma)}{d\sigma} d\sigma\right]. \tag{13}$$

At this point, we still must record the entire history to calculate the airfoil lift, as the integral bounds include $t = 0$. We have only replaced recording the wake vorticity over time (as in UVLM) with recording the foil effective normalwash $v_e^i(t)$ over time. The memory cost (and number of states) is equivalent.

However, the number of states reduces dramatically when we replace the Wagner function with an exponential approximation from Table 1, such as Jones's approximation [20]:

$$\phi(\tilde{t}) \approx 1 + A_{\phi 1} e^{b_{\phi 1}\tilde{t}} + A_{\phi 2} e^{b_{\phi 2}\tilde{t}} = 1 - 0.165 e^{-0.045\tilde{t}} - 0.335 e^{-0.3\tilde{t}}. \tag{14}$$

The Duhamel integral can now be integrated by parts, and exponentials substituted in:

$$\frac{L^i(t)}{L_{\text{qs}}^i} = \frac{1}{v_e^i(t)}\left[\phi(0) v_e^i(t) - \int_0^{\tilde{t}(t)} \frac{d\phi(\tilde{t}-\sigma)}{d\sigma} v_e^i(\sigma) d\sigma\right], \tag{15}$$

$$\frac{L^i(t)}{L_{\text{qs}}^i} = \frac{1}{v_e^i(t)}\left[\phi(0) v_e^i(t) + \int_0^{\tilde{t}(t)} A_{\phi 1} b_{\phi 1} e^{b_{\phi 1}(\tilde{t}-\sigma)} v_e^i(\sigma) d\sigma + \int_0^{\tilde{t}(t)} A_{\phi 2} b_{\phi 2} e^{b_{\phi 2}(\tilde{t}-\sigma)} v_e^i(\sigma) d\sigma\right]. \tag{16}$$

Finally, we can replace the two integral terms in Eq. (16) with $x_{\phi 1}(t)$ and $x_{\phi 2}(t)$, explicitly giving the local lift on each wing section:

$$L^i(t) = \frac{1}{2}\rho c^i C_{l\alpha} v_\perp^i(t)[\phi(0) v_e^i(t) + x_{\phi 1}^i(t) + x_{\phi 2}^i(t)]. \tag{17}$$

The states $x_{\phi 1}^i(t)$ and $x_{\phi 2}^i(t)$ therefore represent the accumulated effect of the wake, and their rates of change can be integrated over time. Unlike in UVLM, the vortex loops from each timestep need not be remembered. Furthermore, unlike in a standard linear Duhamel integral of the Wagner function, the wing velocity $v_\perp^i$ need not be constant magnitude or direction, thereby constituting a linear time-varying (LTV) system.

2. *Circulation*

The circulation of each blade section is derived similarly from the Duhamel integral in Eq. (13), replacing the lift step response $\phi(\tilde{t})$ with the circulation step response $\tilde{\Gamma}(\tilde{t})$. For example, using the $N_\Gamma = 4$ exponential approximation, the circulation reduces to:

$$\Gamma^i(t) = \frac{1}{2} c^i C_{l\alpha}[\tilde{\Gamma}(0) v_e^i(t) + x_{\Gamma 1}^i(t) + x_{\Gamma 2}^i(t) + x_{\Gamma 3}^i(t) + x_{\Gamma 4}^i(t)]. \tag{18}$$

We can now simultaneously solve Eq. (18) and Eq. (2), thereby determining w_n^i and Γ^i, by performing a single $n \times n$ matrix solve to determine the aerodynamic influence of the trailers:

$$\boldsymbol{\Gamma}(t) = \left(\text{diag}\left[\frac{2}{c^i C_{l\alpha}}\right] - \tilde{\Gamma}(0) W_n\right)^{-1} \left[\tilde{\Gamma}(0)\boldsymbol{v}_n(t) + \boldsymbol{x}_{\Gamma 1}(t) + \boldsymbol{x}_{\Gamma 2}(t) + \boldsymbol{x}_{\Gamma 3}(t) + \boldsymbol{x}_{\Gamma 4}(t)\right]. \tag{19}$$

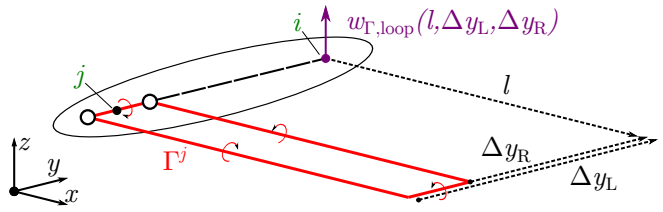

Figure 5. *Vortex Loop Wake* - Downwash at point i along the span, due to a single vortex loop of circulation Γ^j at location j.

3. *State Dynamics*

Using Liebnitz rule, the lift state dynamics can be found by the time derivative of each integral in Eq. (16). The bound $\tilde{t}(t)$ has rate of change of $2v^i_\perp(t)/c$.

$$\dot{x}^i_{\phi 1} = \frac{2v^i_\perp(t)}{c^i}\left[b_{\phi 1}x^i_{\phi 1}(t) + A_{\phi 1}b_{\phi 1}v^i_e(t)\right], \tag{20}$$

$$\dot{x}^i_{\phi 2} = \frac{2v^i_\perp(t)}{c^i}\left[b_{\phi 2}x^i_{\phi 2}(t) + A_{\phi 2}b_{\phi 2}v^i_e(t)\right]. \tag{21}$$

The rates of change of the circulation states are given in a similar form. However, rather than using only independent states for $\tilde{\Gamma}(\tilde{t})$, we reuse the shared poles between the lift and circulation subsystems to obtain better accuracy with the same number of independent states. Given that $b_{\Gamma 1} = b_{\phi 1}$, $b_{\Gamma 2} = b_{\phi 2}$, and both systems share the same input, we can directly convert $x^i_{\phi 1}$ and $x^i_{\phi 2}$ to $x^i_{\Gamma 1}$ and $x^i_{\Gamma 2}$:

$$x^i_{\Gamma 1} = \frac{A_{\Gamma 1}x^i_{\phi 1}}{A_{\phi 1}}, \qquad x^i_{\Gamma 2} = \frac{A_{\Gamma 2}x^i_{\phi 2}}{A_{\phi 2}}. \tag{22}$$

The remaining two circulation states are used as a high-frequency correction to the approximation in Eq. (10). These extra states are only important for fast dynamics, as characterized by the reduced frequency $k = \frac{\omega c}{2U} > 1$. Their time evolutions are given by:

$$\dot{x}_{\Gamma 3} = \frac{2v^i_\perp(t)}{c^i}\left[b_{\Gamma 3}x^i_{\Gamma 3}(t) + A_{\Gamma 3}b_{\Gamma 3}v^i_e(t)\right], \tag{23}$$

$$\dot{x}_{\Gamma 4} = \frac{2v^i_\perp(t)}{c^i}\left[b_{\Gamma 4}x^i_{\Gamma 4}(t) + A_{\Gamma 4}b_{\Gamma 4}v^i_e(t)\right]. \tag{24}$$

D. Unsteady Downwash Correction

Given the difference in wake representation highlighted in Fig. 1, we now derive a small correction term that consolidates the true 3D unsteady wake with the 3D quasi-steady and 2D unsteady wake. This requires an additional state-space system for each blade, namely:

- Two final states x^i_{w1} and x^i_{w2} represent the downwash as if the blade element were alone and of infinite span (Appendix A). These states are later mapped to the full 3D wake using a cross-coupling matrix, giving the downwash onto other elements.

This correction is currently only derived for unswept-wings, allowing for a simpler scalar form.

The primary assumption in our correction is that the unsteady downwash at one part of the wing i is proportional to the downwash states on another part of the wing j (Fig 5). This allows us to record states for every wing section, $O(n)$, rather than every pair of wing sections $O(n^2)$. The contributions of unsteady vortex loops are superimposed in space and integrated in time using a Duhamel integral. See Appendix B for a full derivation.

The effect of this downwash correction is given by three cross-coupling matrices: W_0, W_1, W_2:

$$\boldsymbol{w}_n(t) = W_n\boldsymbol{\Gamma}(t) + \boldsymbol{w}_{\text{correction}} \tag{25}$$

$$= W_n\boldsymbol{\Gamma}(t) + [W_0\boldsymbol{\Gamma}(t) + W_1\boldsymbol{x}_{w1}(t) + W_2\boldsymbol{x}_{w2}(t)]. \tag{26}$$

Matrices W_0, W_1, and W_2 (derived in Appendix B) relate the influence of the unsteady wake at one blade element to the wake at another blade element, and are fit accordingly to the 3D step response. Under steady state, the $W_1\boldsymbol{x}_{w2}(t)$ and $W_2\boldsymbol{x}_{w2}(t)$ exactly cancel $W_0\boldsymbol{\Gamma}(t)$, resulting in the original downwash formulation in Eq. (2).

The state dynamics are given by:

$$\dot{x}^i_{w1} = \frac{2v^i_\perp(t)}{c^i}\left[b_{w1}x^i_{w1}(t) + \frac{2}{c^i}A_{w1}b_{w1}\Gamma^i(t)\right], \tag{27}$$

$$\dot{x}^i_{w1} = \frac{2v^i_\perp(t)}{c^i}\left[b_{w2}x^i_{w1}(t) + \frac{2}{c^i}A_{w2}b_{w2}\Gamma^i(t)\right]. \tag{28}$$

The circulation of each element is then found by adjusting the circulation from Eq. (18) with the downwash in Eq. (26):

$$\boldsymbol{\Gamma}(t) = \left(\text{diag}\left[\frac{2}{c^iC_{l\alpha}}\right] - \tilde{\Gamma}(0)[W_n + W_0]\right)^{-1}[\tilde{\Gamma}(0)(\boldsymbol{v}_n(t) + W_1\boldsymbol{x}_{w1}(t) + W_2\boldsymbol{x}_{w2}(t)) + \boldsymbol{x}_{\Gamma 1}(t) + \boldsymbol{x}_{\Gamma 2}(t) + \boldsymbol{x}_{\Gamma 3}(t) + \boldsymbol{x}_{\Gamma 4}(t)]. \tag{29}$$

E. Reduced State Representation

To avoid overfitting and further reduce the order of the model, we now derive an alternative one-state representation. The simplification requires approximating the step responses $\phi(\tilde{t})$, and $\tilde{\Gamma}(\tilde{t})$ as single exponentials. In this case, we only include one state x^i_ϕ for each blade element that tracks the blade's lift. This single state is then applied to calculate both the lift and circulation, namely:

- The lift is given by a 1-pole state-space system $x^i_{\phi 1}$, following the $N_\phi = 1$ approximation in Table 1.
- Next, the circulation state $x^i_{\Gamma 1}$ is given as a multiplicative gain on lift state $x^i_{\phi 1}$, following the $N_\Gamma = 1$ approximation in Table 1.

The two necessary indicial functions - lift and circulation for a step input in the effective normalwash v_e, are therefore approximated as:

$$\phi(\tilde{t}) \approx 1 + A_\phi e^{b_\phi \tilde{t}} = 1 - 0.5e^{-0.25\tilde{t}}, \tag{30}$$

$$\tilde{\Gamma}(\tilde{t}) \approx 1 + A_\Gamma e^{b_\Gamma \tilde{t}} = 1 - 0.8e^{-0.25\tilde{t}}. \tag{31}$$

Again, we can derive $x^i_{\Gamma 1}(t)$ from $x^i_{\phi 1}(t)$ as in Eq. (22). The lift, circulation, and state dynamics are identical to Section II.C, but all states beyond $x^i_{\phi 1}$ and $x^i_{\Gamma 1}$ are neglected.

F. Lift, Drag, and Added Mass Forces

The scalar lift from Section II.C is rotated by both the blade element motion and downwash to give vectorial lift and induced drag, as consistent with lifting line theory [43]. The total effective wing motion is given as:

$$\boldsymbol{v}^i_{\text{total}} = \boldsymbol{v}^i_{3/4} + \boldsymbol{w}^i + (\hat{\boldsymbol{v}}^i_\perp \times \hat{\boldsymbol{s}}^i)[w^i_{\text{2D}} + w^i_{\text{correction}}], \tag{32}$$

where $\boldsymbol{v}^i_{3/4}$ is the vectorial wing motion at ¾-chord, $\boldsymbol{w}^i$ is the spatial vector downwash from the sum of the horseshoe trailers (Section II.A), $w^i_{\text{correction}}$ is the optional downwash correction (Section II.D), and w^i_{2D} is the additional downwash due to unsteady effects even if the wing were of infinite span. w^i_{2D} is determined by the lift deficit predicted in Eq. (17), and assumed to act normal to the local wake plane [41]:

$$w^i_{\text{2D}} = \phi(0)v^i_e(t) + x^i_{\phi 1}(t) + x^i_{\phi 2}(t) - v^i_e(t). \tag{33}$$

Finally, we assume that the lift force $\boldsymbol{F}^i_L$ acts perpendicular to both $\boldsymbol{v}^i_{\text{total}}$ and the wing sweep $\hat{\boldsymbol{s}}^i$:

$$\boldsymbol{F}^i_L(t) = L^i(t)\Delta s[\hat{\boldsymbol{v}}^i_{\text{total}} \times \hat{\boldsymbol{s}}^i]. \tag{34}$$

Profile drag is neglected in the model for ease of comparison to the UVLM code. However, quasi-steady profile drag is generally easily incorporated as an additional force [32].

The added mass force in full UVLM codes is usually found from the unsteady Bernoulli equation; however, none of the presented states directly translate into the unsteady flow potential. Added mass is therefore instead determined from pre-derived coefficients and known body kinematics, as derived in matrix form by Fossen and Fjellstad [44]. We assume the wing is a flat slender body, meaning that the added-mass coefficients of each section i can be approximated by a flat plate. Coefficients may be derived for any origin point on the blade section.

As an example, the added-mass coefficients below assume body-frame velocity $\boldsymbol{v_b} = [v_1\, v_2\, v_3]^T$ aligned along the chord, span, and chord-normal respectively, taken at the ¾-chord point. Using the notation from Newman [45], the coefficients reduce to:

$$m^i_{33} = \rho\pi K_{\text{am}}\left(\frac{c^i}{2}\right)^2\Delta s, \quad m^i_{35} = m^i_{53} = \frac{c^i}{4}m^i_{33}, \tag{35}$$

$$m^i_{55} = \frac{\pi}{8}\rho\left(\frac{c^i}{2}\right)^4\Delta s + \left(\frac{c^i}{4}\right)^2 m^i_{33}. \tag{36}$$

Correction factor K_{am} compensates for finite aspect ratio effects on the slender body assumption, which Munk [46] gives as $K_{\text{am}} = 0.85$ for $\mathit{AR} = 3$ and $K_{\text{am}} = 0.95$ for $\mathit{AR} = 6$. The general mass matrix for the blade section is given as:

$$M^i_a = \begin{bmatrix} m^i_{11} & m^i_{12} & \cdots & m^i_{16} \\ m^i_{21} & m^i_{22} & \cdots & m^i_{26} \\ \vdots & \vdots & \ddots & \vdots \\ m^i_{61} & m^i_{62} & \cdots & m^i_{66} \end{bmatrix} = \begin{bmatrix} M^i_{11} & M^i_{12} \\ M^i_{21} & M^i_{22} \end{bmatrix}. \tag{37}$$

Block matrix sections M^i_{11}, M^i_{12}, etc. are all 3x3. The added mass coriolis matrix is now derived from M^i_a as:

$$C^i_a = \begin{bmatrix} 0 & -S(M^i_{11}\boldsymbol{v^i_b} + M^i_{12}\boldsymbol{\omega^i_b}) \\ -S(M^i_{11}\boldsymbol{v^i_b} + M^i_{12}\boldsymbol{\omega^i_b}) & -S(M^i_{21}\boldsymbol{v^i_b} + M^i_{22}\boldsymbol{\omega^i_b}) \end{bmatrix}, \tag{38}$$

where S is the skew-symmetric matrix operator, and $\boldsymbol{\omega^i_b} = [\omega^i_1\, \omega^i_2\, \omega^i_3]^T$ is the body-frame rotation vector. Finally, added mass force $\boldsymbol{F^i_a}$ and moment $\boldsymbol{\tau^i_a}$ are given in the body frame by:

$$\begin{bmatrix} \boldsymbol{F^i_a} \\ \boldsymbol{\tau^i_a} \end{bmatrix} = -M^i_a \begin{bmatrix} \boldsymbol{\dot{v}^i_b} \\ \boldsymbol{\dot{\omega}^i_b} \end{bmatrix} - C^i_a \begin{bmatrix} \boldsymbol{v^i_b} \\ \boldsymbol{\omega^i_b} \end{bmatrix}. \tag{39}$$

The added-mass torque τ^i_a includes a Munk moment [45] which is non-physical for airfoils due to the Kutta condition's elimination of the rear stagnation point. This can be corrected by adding a canceling moment about the spanwise axis:

$$\tau^i_{\text{anti-Munk}} = -(m^i_{33} - m^i_{11})v^i_1 v^i_3. \tag{40}$$

III. Flat Elliptic Planform Results

To validate the state-space method, we will first examine four cases and compare with the UVLM code from Zhu et. al. [23]. As the UVLM is used as a validation ground-truth, we use an ultra-fine mesh of 1558 panels, distributed over the top and bottom of the wing surface, dividing the span into 41 blades (Fig. 6b). The state-space systems are simulated in Drake [47], an open-source MATLAB nonlinear control and optimization toolbox.

For ease of comparison with the literature [20], all cases are performed on an elliptic planform wing of $\mathit{AR} = 3$, sheared to obtain a straight ¼-chord line (Fig. 6). The four cases are:

- Impulsively started wing
- Surge oscillations
- Pitch oscillations
- Large amplitude heave/pitch oscillations

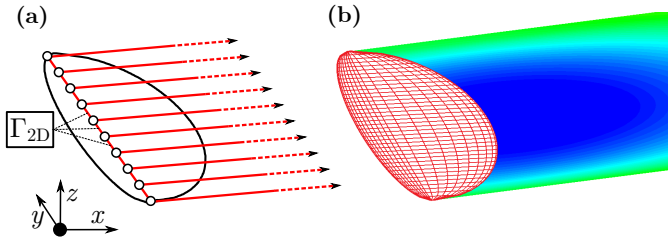

Figure 6. *Elliptic Planform* - Left (a): Model of elliptic planform wing, consisting of 9 blade elements and their respective state-space systems. Right (b): Unsteady vortex lattice method (UVLM) visualization for an impulsively started elliptic planform wing, wake colored as panel dipole strength.

A more complicated trajectory, with bird-like flapping, can be found in Section IV, and a brief comparison to experiments in Section V. We will compare three different models:

- A 6-state solution per blade element, using $N_\phi = 2$, $N_\Gamma = 4$ (with two ϕ states repeated), and the unsteady downwash correction $N_w = 2$.
- A 1-state solution per blade element, using $N_\phi = 1$, $N_\Gamma = 1$ (sharing the ϕ state), and no downwash correction.
- A quasi-steady/added-mass formulation (QS,AM): namely assuming that both the lift and circulation are at steady-state at any given time ($\tilde{\phi}(\tilde{t}) = \tilde{\Gamma}(\tilde{t}) = 1$, so no states required), but including the added-mass forces from Section II.F.

For all cases, the number of blade elements is fixed at $n = 9$. However, we also present convergence tests over n for the surge case. The blades are spaced using cosine spacing [25], but other discretization choices could be used: for example, the natural location of joints on a biological wing.

A. Impulsive Start of Elliptic Planform

Figure 7 illustrates our first validation case, an impulsive start with angle-of-attack of $\alpha = 5°$. For this case, our solution can be compared exactly to the analytic work of Jones [20]. Jones provides two analytic solutions - one derived from an assumed elliptic load distribution, and another corrected for initial conditions. The error between Jones's two solutions gives a good estimate for acceptable variation. The predicted lift from our proposed unsteady state-space models lie nicely between Jones and UVLM, and almost exactly agrees in the steady state to Prandlt's analytic lifting line theory [35].

For the step response transient, rather than maintaining the lift dependency on angle-of-attack, we normalize the total lift as wing lift coefficient $C_{L\alpha}(t)$:

$$C_{L\alpha}(t) = \frac{F_z(t)}{\frac{1}{2}\rho U^2 S \sin\alpha}, \tag{41}$$

where F_z is the global frame vertical force. A lifting surface will generally have less lift than a lifting line, leading to an unavoidable discrepancy between Jones/Prandtl and UVLM. Hoerner [31] proposes a suitable correction factor:

$$\frac{C_{L\alpha,\text{surface}}}{C_{L\alpha,\text{line}}} = \frac{(2\pi)^{-1} + (\pi\mathit{AR})^{-1}}{(2\pi)^{-1} + (\pi\mathit{AR})^{-1} + \frac{K\pi}{180}\mathit{AR}^2}. \tag{42}$$

Hoerner claims $K \approxeq 9$ for best agreement with experiments. For consolidating the difference between analytic lifting line (Jones/Prandtl) and the UVLM, we use $K = 13.5$. The circulation Γ^i and downwash $\boldsymbol{w}^i$ of each section are similarly scaled by the same gain. Once the correction factor is applied, all solutions agree in steady state (Fig. 7).

In fact, the state-space model under steady state ($t \to \infty$) reduces to the numerical solution [29] of the Prandtl lifting line problem, with

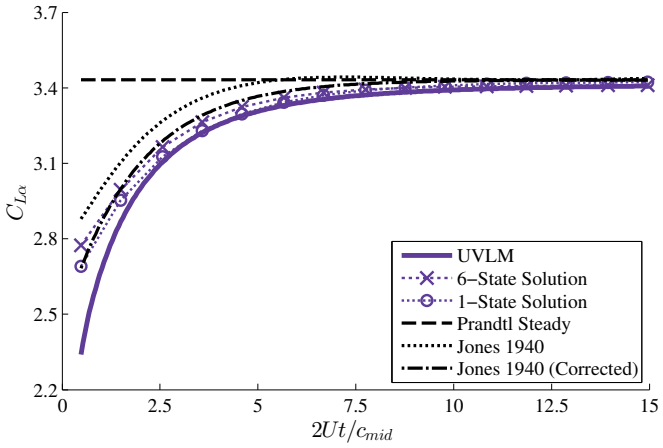

Figure 7. ***Impulsive Start*** **- Two state-space solutions, using $n = 9$ blade elements along the span, validated against Jones [20] and an unsteady vortex lattice method (UVLM) [23]. Results are for an impulsively started wing of elliptic $\mathcal{AR} = 3$ planform.**

n steady horseshoe vortices. Specifically, when all states reach steady-state, $\dot{x}_\phi = 0$, from which we can derive:

$$x^i_{\phi 1} = -A_{\phi 1} v^i_e, \quad x^i_{\phi 2} = -A_{\phi 2} v^i_e \tag{43}$$

and similarly for the circulation states. Therefore, the steady-state lift and circulation are reduced to their familiar expressions:

$$L^i(t) = \frac{1}{2}\rho c^i C_{l\alpha} v^i_\perp v^i_e [\phi(0) - A_{\phi 1} - A_{\phi 2}] = \frac{1}{2}\rho c^i C_{l\alpha} v^i_\perp v^i_e, \tag{44}$$

$$\Gamma^i(t) = \frac{1}{2} c^i C_{l\alpha} v^i_e [\tilde{\Gamma}(0) - A_{\Gamma 1} - A_{\Gamma 2} - A_{\Gamma 3} - A_{\Gamma 4}] = \frac{1}{2} c^i C_{l\alpha} v^i_e, \tag{45}$$

which also happens to be the governing equations for a quasi-steady model. If the unsteady downwash correction is included (Appendix B), the aerodynamic influence matrix similarly reduces to lifting line under steady state, so the steady downwash is equivalent. Our choice of $n = 9$ blade elements results in only 0.2% error as compared to the Prandlt lift, and Prandlt's solution is exactly reconstructed as $n, t \to \infty$.

B. Surge Oscillations

Surge oscillations, which directly vary the flow speed $v_\perp(t)$, showcase the LTV (linear time-varying) nature of the model. We again start the wing at $\alpha = 5°$, but give it a time-varying velocity of:

$$v(t) = U + U\lambda \sin \omega t, \tag{46}$$

where λ is the normalized surge velocity amplitude, and ω is the angular frequency. We non-dimensionalize ω as the mid-span reduced frequency:

$$k_{\text{mid}} = \frac{\omega c_{\text{mid}}}{2U}. \tag{47}$$

Additionally, we normalize the relevant simulation outputs, total force and mid-span circulation, as:

$$C_{D\alpha}(t) = \frac{F_x(t)}{\frac{1}{2}\rho U^2 S \sin\alpha}, \tag{48}$$

$$C_{\Gamma\alpha}(t) = \frac{\Gamma_{\text{mid}}(t)}{2Ub \sin\alpha}. \tag{49}$$

The $\lambda = 0.5$ and $k_{\text{mid}} = 2$ case is illustrated in Fig. 8a, with time normalized by the oscillation period T. Note the significant phase difference between the lift and circulation, indicating the importance of added-mass forces. The lift is also clearly non-sinusoidal; the peaks skew forwards in time, as expected from the LTV system. The lift and drag match exceptionally well with the UVLM simulation for both

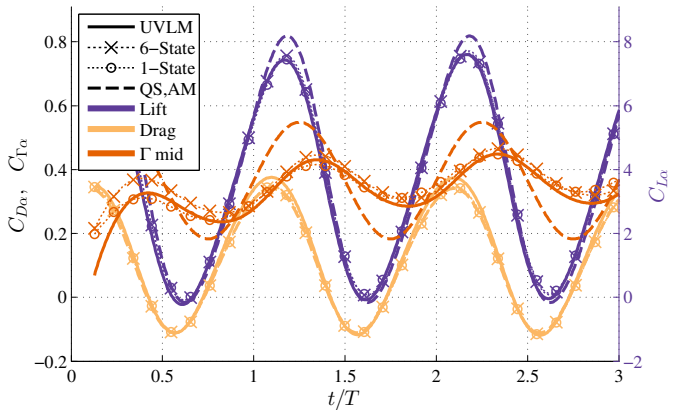

a) ***Surge Oscillation Example*** **- Surge oscillation frequency $k_{\text{mid}} = 2$. Lift scaled down for ease of comparison, as indicated by right y-axis.**

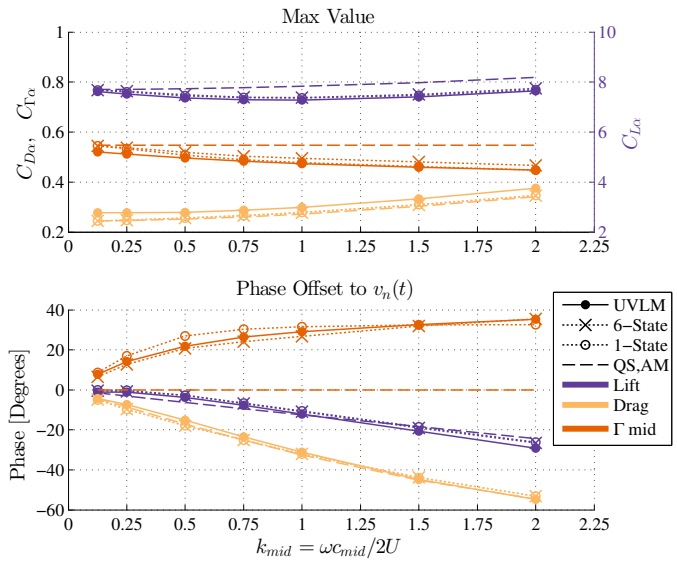

b) ***Parameter Sweep*** **- Amplitude and phase in surge response, as compared to $v_n(t)$ at mid-span.**

Figure 8. ***Surge Oscillations*** **- Lift, drag, and circulation for surge oscillations on a elliptic planform wing of $\mathcal{AR} = 3$, with angle of attack $\alpha = 5°$, and sinusoidal surge amplitude $\lambda = 0.5$.**

state-space models, meaning the $N_\phi = 1$ model is likely sufficient for control.

In terms of circulation, there exists a small discrepancy between the two state-space models, as the high reduced frequency requires better fidelity of capturing the short-timescale circulation response. This is especially pronounced at the peaks and troughs of each cycle, where the wing velocity changes quickly, therefore sweeping a broader band of the frequency spectrum of the state-space approximation to $\tilde{\Gamma}(\tilde{t})$.

A parametric study over k_{mid} can be found in Fig. 8b, again $\lambda = 0.5$. While the response is not purely sinusoidal, we reduce the data by comparing maximum peak value and peak phase offset as a stand-in for magnitude and phase for ease of comparison and data reduction:

$$C_{L\alpha,\text{Peak}} = \max[C_{L\alpha}(t)], \tag{50}$$

$$C_{L\alpha,\text{Phase}} = \frac{2kU}{c_{\text{mid}}}\Big(\text{argmax}[C_{L\alpha}(t)] - \text{argmax}[v_n(t)]\Big) \mod 2\pi. \tag{51}$$

At higher reduced frequencies ($k_{\text{mid}} > 1$), the added mass force begins to compete with the circulation-based lift, as indicated by the decreasing circulation magnitude and decrease in phase of the lift force (Fig. 8b). Added mass force is proportional to acceleration, so we expect the lift phase to reach $-90°$ at $k_{\text{mid}} \gg 1$.

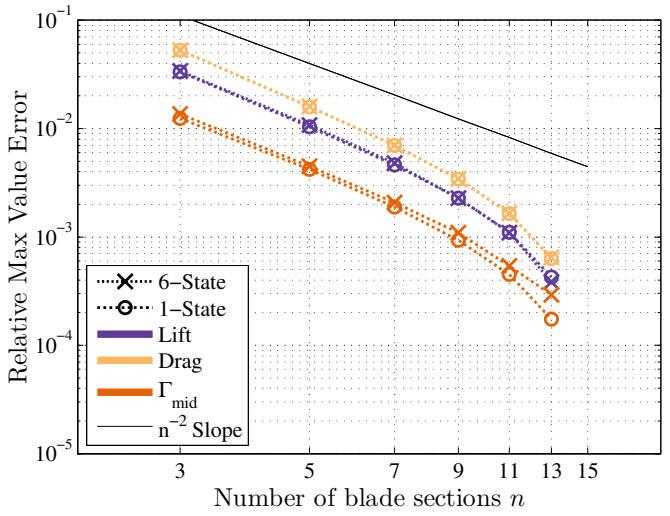

Figure 9. ***Surge Oscillation Convergence*** **- Both state-space models converge at second order for all three measured peak quantities $C_{L\alpha,\text{Peak}}$, $C_{D\alpha,\text{Peak}}$ and $C_{\Gamma\alpha,\text{Peak}}$. Error compared against same calculation at $n = 15$, all axes are logscale.**

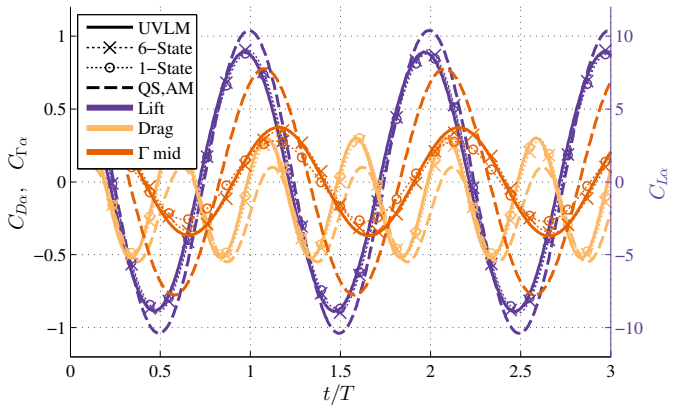

a) ***Pitch Oscillation Example*** **- Pitch oscillation frequency $k_{\text{mid}} = 2$. Again, lift is scaled as indicated by right y-axis.**

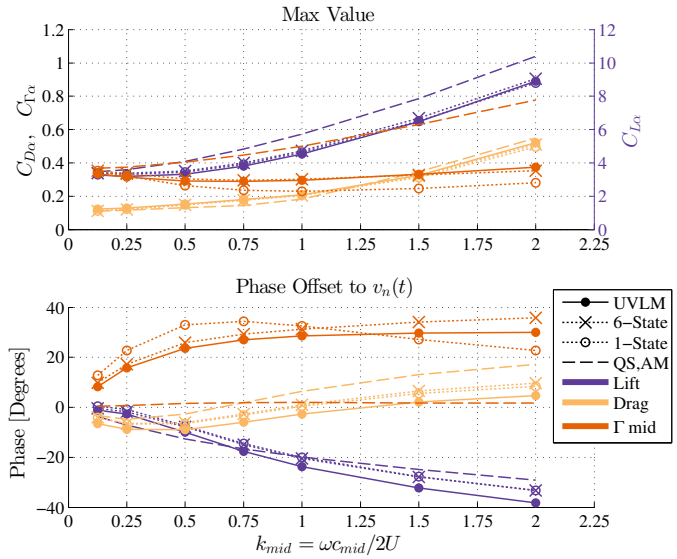

b) ***Parameter Sweep*** **- Amplitude and phase in pitch response, as compared to $v_n(t)$ at mid-span.**

Figure 10. ***Pitch Oscillations*** **- Lift, drag, and circulation for pitch oscillations on a elliptic planform wing of $\mathcal{AR} = 3$, with sinusoidal pitch amplitude $\alpha_{\text{max}} = 5°$.**

The parametric study confirms that both state-space methods are roughly equivalent for force prediction, but the additional states are required for predicting the circulation. For example, at all tested frequencies both state-space methods have max phase error of roughly 3° on the predicted lift and drag forces. Including the extra states lowers the maximum circulation phase error from 5° to 2° over the frequency sweep.

The peak height error is also small over the tested frequency range. The lift and circulation peak height error remains below 5% for both state-space methods. The drag peak error, however, grows to 12% at low frequencies as we approach the expected steady error between the lifting line and lifting surface codes.

In robust control theory, a model with the stated 5° phase error and 12% gain are well within standard margins [48] for maintaining stability despite unmodeled dynamics. Therefore, in the surging case, the state-space models and UVLM code can be considered interchangeable for the purpose of control design.

The quasi-steady/added-mass model (QS,AM) unsurprisingly fails at higher frequency to capture the circulation, and shows consistent error in the force predictions. However as the frequency increases, the circulation-based lift is dwarfed by the added-mass forces, meaning that the force performance is better than the circulation error would imply. This is a general theme throughout oscillatory solutions for foils: low and high reduced frequencies are easy to model ($k_{mid} \ll 1$ and $k_{mid} \gg 1$), but the mid-range frequencies found in flapping flight require detailed analysis of the wake, either as panel methods or state-space solutions.

Finally, given that the state-space model and UVLM predict slightly different maximum lift, drag, and circulation due to lifting surface effects, the state-space model does *not* converge to UVLM as the number of blade elements in increased. However, the solution does converge stably to a fixed value at second order ($O(n^{-2})$), even in the unsteady surge case. Figure 9 illustrates the error between the calculated $C_{L\alpha,\text{Peak}}$, $C_{D\alpha,\text{Peak}}$ and $C_{\Gamma\alpha,\text{Peak}}$ and the same calculation performed with 15 blade elements. The accelerating convergence beyond $n > 11$ is likely due to the cosine spacing of the blades.

For the purposes of control, this additionally illustrates that the number of states can be further reduced by changing the number of blade elements. If a robust control algorithm can handle an additional 2% of magnitude error, the number of blade elements can safely be reduced to only $n = 5$.

C. Pitch Oscillations

High frequency $k_{\text{mid}} = 2$ pitching results can be found in Fig. 10a. In this case, the $\mathcal{AR} = 3$ elliptic wing is towed at steady velocity while pitching about its ¼-chord axis:

$$\theta(t) = \alpha_{\text{max}} \sin \omega t, \tag{52}$$

where the amplitude of oscillation $\alpha_{\text{max}} = 5°$. Added-mass forces are again a substantial portion of the force at this frequency, validating both the unsteady lifting line and added mass formulations. We normalize all global-frame forces F_x, F_z and circulation using α_{max} when calculating $C_{L\alpha}$, etc.

Similar to the surge cases, both state-space models perform equivalently when predicting the lift force. The circulation is best captured by the model with the additional states.

An analogous parametric study over k_{mid} can be found in Fig. 10b. Here, the circulation does not decrease with increasing k_{mid}; the oscillating airfoil has pitch-rate-dependent circulation [33] that increases with frequency. Additionally, the lift phase asymptote at high frequency is not −90°, given that the added mass forces are proportional to $\dot{v}_n$ evaluated at ½-chord rather than at ¾-chord.

In comparison to the surge study, the pitching wing predictions do have slightly more error due to the breakdown of the locally flat wake

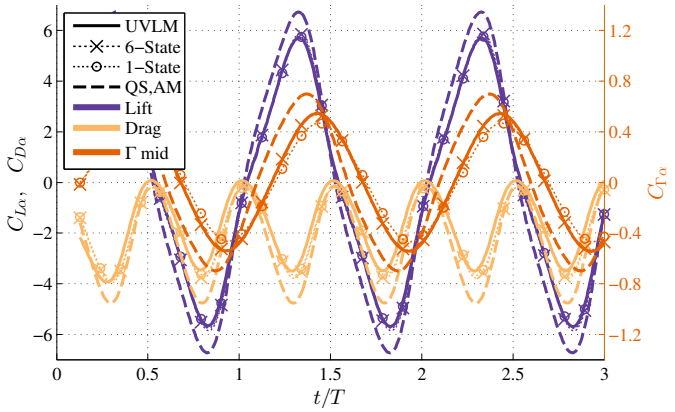

a) *Force and Mid-span Circulation* - Lift, drag, and mid-span circulation for heave-pitch oscillations at $St = 0.3$.

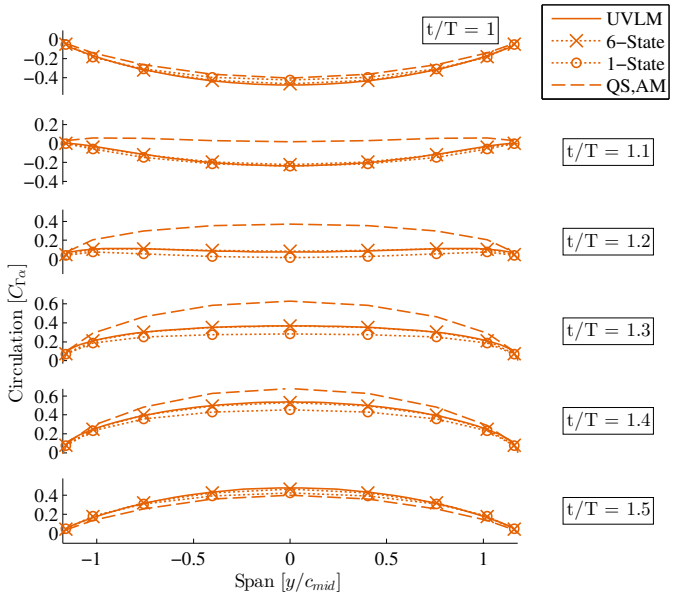

b) *Dynamic Circulation Distribution* - Circulation distribution over the wingspan at select timesteps, illustrating a quarter-cycle.

Figure 11. *Heave-Pitch Oscillations* - Heave-pitch oscillations with $St = 0.3$, $h/c_{\text{mid}} = 0.75$, $\alpha_{\text{max}} = 15^\circ$ on an elliptic planform wing of $\mathcal{AR} = 3$.

assumption. In both state-space models, the peak lift and drag errors reach 6% and 9% respectively, with roughly 5° of phase error each. Again, including the extra circulation states lowers the circulation error from 25% at 9° phase error to 7% with 6° phase error.

Again, ignoring all wake states in a quasi-steady/added-mass model performs worst; at mid-frequency $k_{mid} = 0.75$, it over-predicts the lift by 27% and thrust by 20%. Similar to the surge cases, quasi-steady/added-mass fails to capture the circulation as frequency increases.

D. Heave-Pitch Oscillations

Heave-pitch results on the elliptic planform can be found in Fig. 11a. While not a truly three-dimensional flapping motion, this case illustrates the fidelity of the method in multiple aspects of flapping flight; namely, high-amplitude heave and pitch on a finite aspect-ratio wing.

The heave and pitch motions are given as:

$$z(t) = h\cos\omega t, \tag{53}$$

$$\theta(t) = \theta_{\text{max}}\sin\omega t. \tag{54}$$

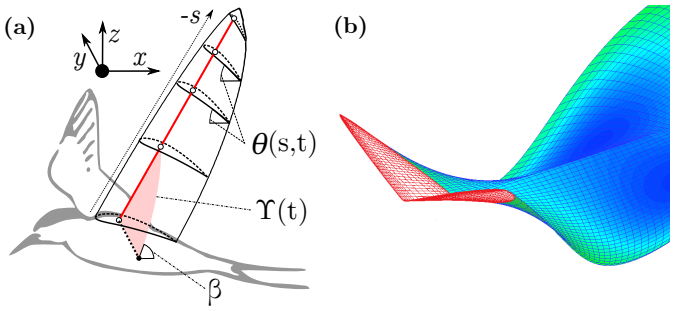

Figure 12. *Flapping Trajectory* - Left (a): Variable definition of spanwise twist $\theta(s,t)$, time-varying dihedral $\Upsilon(t)$, and stroke angle β in state-space model. Right (b): UVLM visualization of wake of a flapping wing with both spanwise twisting and tilted stroke angle, wake colored as dipole strength.

Pitching amplitude θ_{max} is determined by setting the geometric angle-of-attack $\alpha_{\text{max}} = 15^\circ$ at the middle of the downstroke:

$$\theta_{\text{max}} = -\arctan\frac{\omega h}{U} + \alpha_{\text{max}}. \tag{55}$$

Instead of using the reduced frequency k_{mid}, heave-pitch motions are traditionally non-dimensionalized using the heave-to-chord ratio h/c_{mid} and the Strouhal number St:

$$St = \frac{h\omega}{\pi U} = k_{\text{mid}}\frac{h}{c_{\text{mid}}}\frac{2}{\pi}. \tag{56}$$

Flapping foils typically exhibit best thrust efficiency at $0.2 \leq St \leq 0.4$ [49]. For the purposes of validating the method, we will investigate the case of $St = 0.3$ and $h/c_{\text{mid}} = 0.75$, making $k_{\text{mid}} \approx 0.628$ and $\theta_{\text{max}} \approx 28^\circ$.

Similar to the surging and pitching cases, the lift and drag predictions by the two state-space models are largely equivalent, and reliably predict the total force on the flapping wing. The mid-span circulation is best reproduced by the additional states. The model performs again reliably despite the large wake inclination and heave amplitude of $h/c_{\text{mid}} = 0.75$, given the locally linear wake geometry. Normalized foil rotation reaches a maximum of $\dot{\theta}_{\text{max}}c_{\text{mid}}/(2U) = 0.31$, or equivalently, an additional 18° angle of attack between ¼-chord and ¾-chord.

A detailed look at the wing circulation distribution is presented in Fig. 11b. Unlike the predictions by Jones [20], the heaving/pitching elliptic planform wing does not maintain an elliptic circulation distribution. The wing tips exhibit faster dynamics than the mid-span, most easily seen at $t/T = 1.2$. While both state-space models demonstrate equivalent performance predicting the total lift and drag, the extra states are clearly required to correctly track the circulation distribution (and thereby the wing loading).

It is surprising that the 1-state model can correctly predict the drag even with a poor circulation distribution. However, the dominant drag in this case is not the induced drag due to downwash, but instead the drag and thrust due to the lift tilted by the wing motion. Therefore, both state-space methods can easily have similar lift and drag yet different circulation distributions.

IV. Flapping/Twisting Results

Finally, we illustrate a complex bird-like flapping trajectory on a wing of finite aspect ratio, fully showcasing the predictive performance of the method. The wing consists of two independently flapping wings (i.e. shoulder joints), with total $\mathcal{AR} = 6$ and an elliptic planform with straight quarter-chord line (Fig. 12).

First, we twist each wing about the y axis to keep the instantaneous angle of attack of each wing within the linear range. The twist is sinusoidal in time, and linearly increases from midspan to tip:

$$\theta(s,t) = \frac{|s|}{s_{\text{tip}}}\theta_{\text{max}}\sin(\omega t). \tag{57}$$

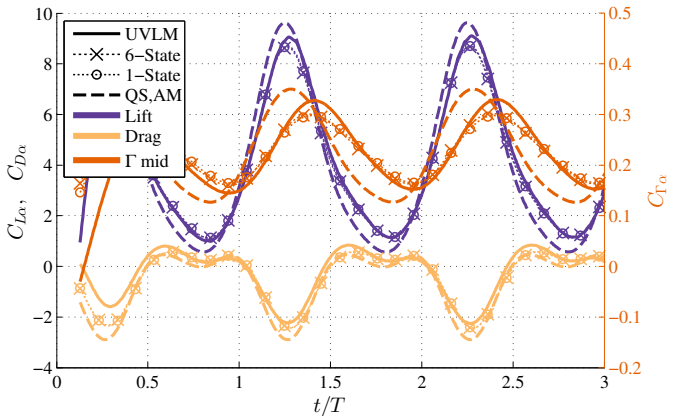

a) ***Force and Mid-span Circulation*** **- Lift, drag, and mid-span circulation for a flapping wing.**

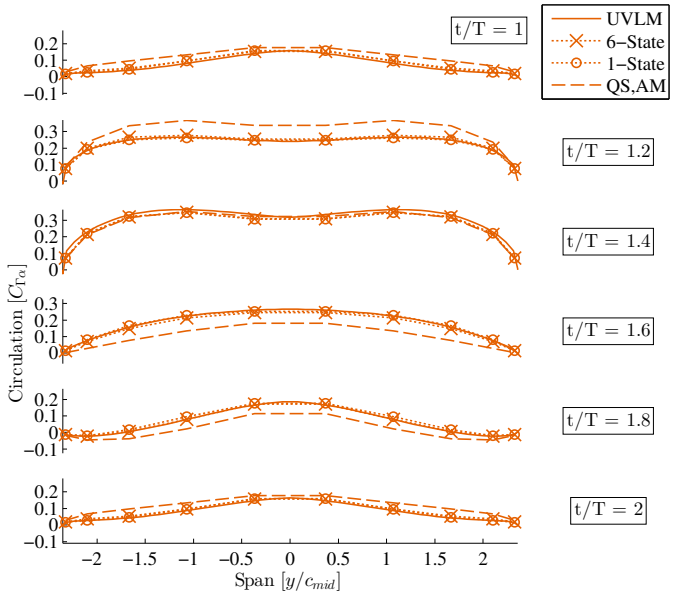

b) ***Dynamic Circulation Distribution*** **- Circulation distribution over the flapping wing at select timesteps.**

Figure 13. ***Flapping Wing Trajectory*** **- Flapping elliptic planform wing of $\mathcal{AR} = 6$. Flapping trajectory includes a tilted stroke angle $\beta = 75°$, wingtip maximum twist of $\theta_{\max} = 30°$, and flapping dihedral amplitude of $\Upsilon_{\max} = 30°$.**

Next, we apply a flapping rotation about x as a dihedral angle Υ:

$$\Upsilon(t) = \Upsilon_{\max}\cos(\omega t). \tag{58}$$

Finally, we also tilt both the wing and stroke angle β [12] around the y axis, such that the wing moves forwards during the downstroke, causing a surging motion of the wingtip. The flapping frequency, again determined from a Strouhal number, is defined using the vertical excursion of the wingtip [50]:

$$St = \frac{\omega}{\pi U} s_{\text{tip}} \cos\Upsilon_{\max}\cos\beta. \tag{59}$$

Overall, the combination of large amplitude flapping $\Upsilon_{\max}$ and a non-vertical stroke angle β means that the wing tip moves both vertically (dynamic dihedral) and fore-aft (dynamic sweepback) relative to the flow, similar to the motion investigated in [51].

An example case of $St = 0.3$, $\Upsilon_{\max} = 30°$, $\beta = 75°$, and $\theta_{\max} = -30°$ is illustrated in Fig. 13. For this trajectory, the maximum and minimum geometric angle-of-attack at ¾-chord is 26.1° and −8.5° respectively, well within reasonable range for previously performed flapping flight studies [2]. To avoid placing a control point at the discontinuity at mid-span, we increase the number of panels to $n = 10$ and use a spline interpolant to recover the mid-span circulation.

The lift and drag of both state-space models agree exceptionally well with the UVLM code (Fig. 13a), with the additional states only marginally increasing the accuracy. The peak lift error reaches only 4.7% for the 6-state and 4.4% for the 1-state, and peak drag error of 7.9% for both state-space models.

The mid-span circulation peak error is slightly larger at 8.4% for the 6-state and 9.6% for the 1-state model. Understandably, the circulation distribution is difficult to capture directly at the mid-span discontinuity, and the error decreases closer to the wingtips (Fig. 13b). Accordingly, at the node $s = 1.06$ the error drops to 3.6% and 5.6% for the two models respectively.

In this flapping case, the reduced-order model of $N_\phi = N_\Gamma = 1$ is therefore clearly sufficient for recovering the dynamics of the system. The accuracy does not improve substantially by increasing the number of states, indicating that the dominant error is likely unmodelled, and therefore perhaps due to wake deflection or lifting surface effects.

V. Model Limitations and Comparison to Experiments

As discussed throughout the previous sections, the presented model is only accurate for at most a subset of the flows that are well-predicted by UVLM. These flows must remain attached, must only shed vorticity from the trailing edge, and must retain consistency with lifting line theory. Therefore, the following effects are *not* included

- Flow separation from the trailing edge, a viscous effect.
- Leading edge vortex shedding, as the loss of leading edge suction and multiple vortex systems are not easily modeled with classic UVLM.
- Wake-capture [42], where the wing intersects its own wake, voiding the Duhamel formulation.
- Fast foil rotation beyond the tested range, where we expect the Duhamel superposition to no longer accurately predict the force. The wake history effects may decay at a rate other than $\phi(\tilde{t})$, given the rotated body boundary conditions, and thereby alter the state dynamics.
- Oscillations approaching the scale of the chordlength, which require a lifting surface to resolve the downwash variations over the chord [21].
- Wings of low aspect-ratio, where even in the steady case, a lifting line approximation is unwarranted [35].

Therefore, the presented state-space model is well-suited for flows where the flapping frequency is high enough to avoid separation, but not hovering flight where stable LEVs become a dominant lifting method and the wing advancement is too small justify evaluating the downwash at a single point. Additionally, while the Duhamel integral allows for an inclined wake, it still assumes low wake curvature.

As an example, we now compare the presented model to the finite aspect-ratio experiments results of Scherer [24]. Scherer himself presents a model to predict the thrust from his experiments, but similar to [20], does not account for a variable spanwise circulation distribution. Given that we are now comparing to experiment, we add simple sectional viscous drag, oriented parallel to $\mathbf{v}^{\mathbf{i}}_{\perp}$, of $C_{d0} = 0.057$ as reported by Scherer's static foil tests.

Figure 14 illustrates the mean thrust for a heave-pitch motion of a rectangular planform wing of $\mathcal{AR} = 3$, with the pivot moved to the ¾-chord point. The phase delay ψ between heave and pitch, varied from 15° to 105°, is defined by:

$$z(t) = h\cos\omega t, \tag{60}$$

$$\theta(t) = \theta_{\max}\cos(\omega t + \psi). \tag{61}$$

A phase delay of $\psi = 90°$ and switching the sign of $\theta_{\max}$ recreates the same motion as Section III.D. Scherer [24] limits his experiment

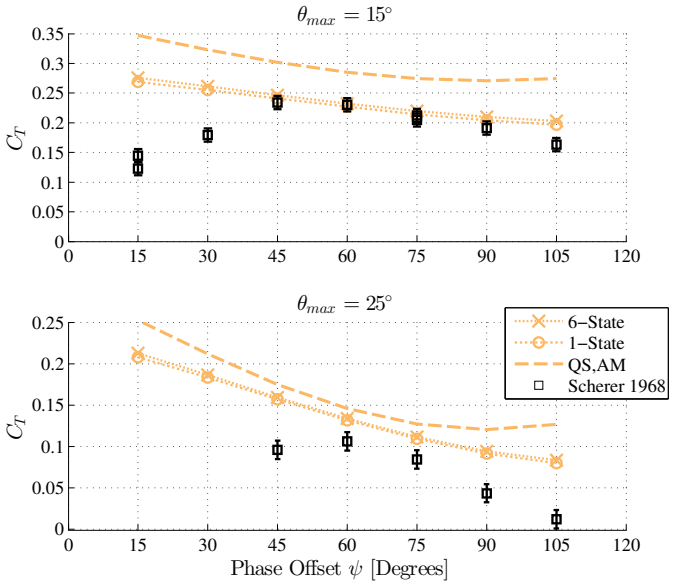

Figure 14. ***Comparison to Scherer [24] Experiments*** **- Mean thrust for a rectangular planform wing of $\mathcal{AR} = 3$, pitching and heaving about the ¼-chord line, for various phase offsets and pitch amplitudes. Model predicts thrust accurately (top) given low peak angle-of-attack and minimal LEV effects.**

parameters to lower Strouhal numbers than typical for flapping flight [52], so we compare against his highest Strouhal number $St = 0.2$ cases ($k_{\text{mid}} = 0.52$), with heave amplitude $h/c = 0.6$.

For the cases of $\theta_{\text{max}} = 15°$, the thrust coefficient is well-predicted by both state-space models for phase shifts between $45°$ and $90°$, which corresponds to trajectories with low peak angles of attack $\alpha_{3/4} < 25°$. Motions with phase shifts below $45°$, however, stall the wing, and a dynamic stall model is therefore required.

At the larger pitch amplitude $\theta_{\text{max}} = 25°$, the peak angle of attack decreases as the wing roughly feathers to the flow. The thrust is therefore unsurprisingly smaller. However, the state-space model performs poorly, as the increased wing rotation rate promotes LEV shedding [14] and thereby a loss of leading edge suction.

In other words, the proposed state-space model captures the reduction in lift due to trailing edge vortex shedding but nothing more; precisely as promised from unsteady lifting line theory. Augmentation by other state-space models for LEV [18, 17] and trailing edge separation [41, 17] would be required to successfully model full dynamic stall.

In all experiment cases, the quasi-steady/added-mass analysis overpredicts the thrust, and our model significantly improves the thrust prediction. The attractiveness of our model is therefore its UVLM-like performance, adapted to a state-space framework plausible for control, in flapping wing regimes of important biological and engineering interest.

VI. Conclusions

The proposed method integrates low-order state-space models, distributed over a wing, to adapt the well-known unsteady lifting line theory into a minimal information framework. These models can be as simple as a single state that adds wake-induced dynamics onto each blade element, without requiring a full record of the wake history in time. Unlike traditional flutter models, these state-space systems work admirably even for situations that are clearly nonlinear, such as large amplitude variations in heave, surge, and twist; provided that the wing performance is well-predicted by the standard assumptions of unsteady lifting line theory. Control of flapping wings, expertly performed by nature, requires models that quickly and accurately predict the wake effects of these large wing motions.

The presented state-space system can be derived from exponential fits to the step response of each blade section, later combined to give the 3D wake. Many such approximations exist, depending on the fitting parameters or specific airfoil section. This paper derives two models and validates their performance in detail:

- A simple one-state per blade element ($N_\phi = N_\Gamma = 1$, with the single state repeated for both lift and circulation), and
- A six-state model ($N_\phi = 2, N_\Gamma = 4$, with two states repeated, and a $N_w = 2$ wake correction).

These models are then compared to an unsteady vortex lattice method (UVLM), presented in Zhu et. al. [23], which includes both lifting surface and full wake history effects. We analyze four simple cases to validate the method: a step increase in velocity, surge oscillations, pitch oscillations, heave/pitch oscillations. Subsequently, we analyze a complex wing trajectory that includes flapping, surging, and twisting in combination. Finally, we compare to the flapping wing experiments of Scherer [24] to illustrate the limitations of the model as dependent on the wing motion.

For most of the inviscid cases presented, the single-state method captures enough of the system dynamics for confident control system design. For example, assuming a large robustness tolerance of 20% magnitude and $10°$ phase, a single-state method adequately predicts the lift, drag, and circulation for the tested cases of surging, heave/pitching, and flapping. The additional states, and the unsteady downwash correction, improve the accuracy of the dynamic circulation distribution, but have little effect on the total lift and drag predictions and are only truly necessary for fast pitching motions at $k_{\text{mid}} > 1$. As the state-space models require no fit to provide predictive results (purely analytic), the models can also be used for early system design.

In comparison to experiments, the model predictions hold for well-behaved flows without LEV shedding, stall, or wake-capture. Similar to UVLM, these phenomena are not captured by the model, and require integration with other state-space systems from the literature [16, 17, 18].

Overall, simplifying the unsteady wake into a compact state-space model along the lifting line provides a starting point for active control of flapping wings. We expect even better results by allowing the system matrices, such as added-mass, blade lift behavior, and wake cross-coupling, to be fit to experiments and the inclusion of new developing models for dynamic stall, thereby enabling further refinement of model-based control schemes.

Appendix

A. State Space Model for 2D Downwash

First, we track the downwash from a single starting vortex on a wing of infinite span, later correcting the wake to be 3D. This requires an exponential approximation to the 2D step response $w_{\Gamma,2\text{D}}(\tilde{t})$, equivalently, the downwash due to a single wake vortex:

$$w_{\Gamma,2\text{D}}(t) = \frac{dw_{2\text{D}}}{d\Gamma} = -\frac{1}{2\pi l(t)} \approx \frac{2}{c}\left(A_{w1}e^{b_{w1}\tilde{t}} + A_{w2}e^{b_{w2}\tilde{t}}\right). \tag{62}$$

The length $l(t)$ is defined as the distance between the effective control point and the wake vortex (Fig. 5). Jones approximates $l(t)$ as $l(t) \approxeq Ut + c/2$ [20].

The extra inclusion of $2/c$ in Eq. (62) allows A_{w1} and A_{w2} to independent of the local chord. Constants A_{w1} and A_{w2} are derived from Garrick's [53] approximation to $\phi(\tilde{t})$:

$$\phi(\tilde{t}) \approx 1 - \frac{2}{4 + \tilde{t}} \tag{63}$$

Solving for $\tilde{t}$ and plugging into $w_{\Gamma,2\text{D}}(t)$ we achieve:

$$A_{w1} = \frac{1}{4\pi} A_{\phi 1} \exp(-3b_{\phi 1}) = -0.0150 \tag{64}$$

$$A_{w2} = \frac{1}{4\pi} A_{\phi 2} \exp(-3b_{\phi 2}) = -0.0656 \tag{65}$$

$$b_{w1} = b_{\phi 1} = -0.0450, \quad b_{w2} = b_{\phi 2} = -0.3000 \tag{66}$$

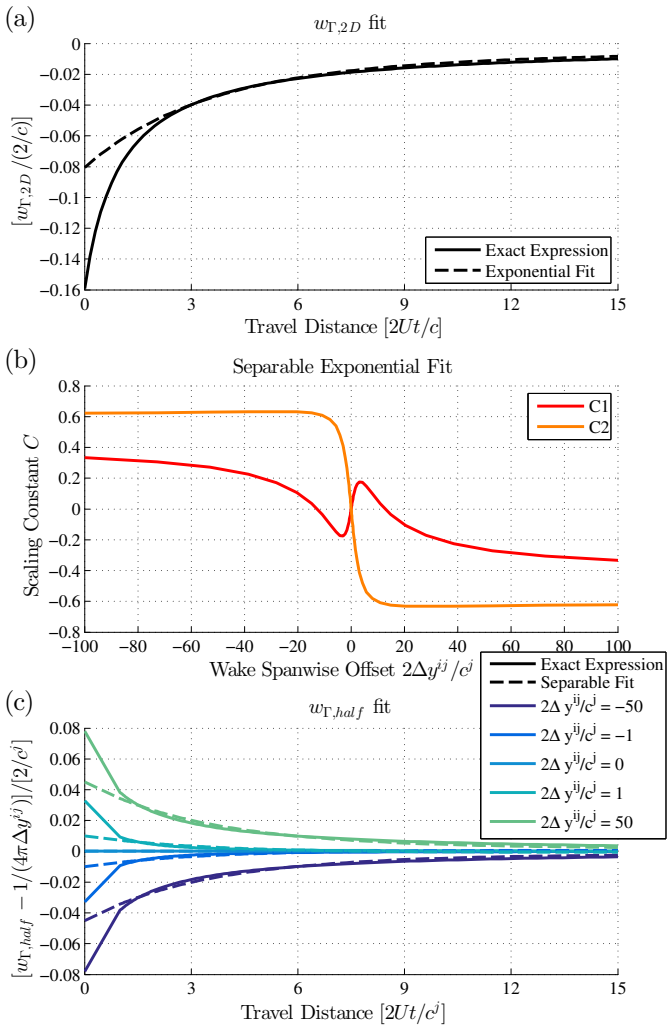

Figure 15. ***Unsteady 3D Wake Correction*** **- (a) Exponential fit for the unsteady wake-induced downwash on a 2D wing, given a step input in airfoil circulation. (b) Scaling constants for each exponential to map to a full 3D wake. (c) Downwash from the 3D wake, as appoximated by a separable sum of exponentials.**

The exponential approximation to $w_{\Gamma,2D}(\tilde{t})$ is illustrated graphically in Fig. 15a. Constants A_{w1}, A_{w2}, b_{w1}, and b_{w2} could alternatively be taken as an exponential fit to $w_{\Gamma,2D}(\tilde{t})$, but the re-use of the exponential fit to $\phi(\tilde{t})$ ensures similar time-scale behavior as other parts of the state-space system.

The states tracking the 2D wake now represent a new Duhamel integral:

$$w^i_{2D}(t) = w_{\Gamma,2D}(\tilde{t})\Gamma^i(0) + \int_0^{\tilde{t}(t)} w_{\Gamma,2D}(\tilde{t}-\sigma)\frac{d\Gamma^i(\sigma)}{d\sigma}d\sigma \quad (67)$$

$$= w_{\Gamma,2D}(0)\Gamma^i(t) - \int_0^{\tilde{t}(t)} \frac{dw_{\Gamma,2D}(\tilde{t}-\sigma)}{d\sigma}\Gamma^i(\sigma)d\sigma \quad (68)$$

$$\approx \frac{2[A_{w1}+A_{w2}]}{c^i}\Gamma^i(t) + x^i_{w1}(t) + x^i_{w2}(t). \quad (69)$$

The rate of change of these wake states are again given by Duhamel integral, as stated in Eq. (27) and Eq. (28).

B. Unsteady 3D Downwash Correction

We now discretize the wake along each blade element, creating a set of rectangular vortex loops (Fig. 5). The downwash of one such loop j, with the left and right legs offset to location i by Δy_L and Δy_R is given as:

$$w_{\Gamma,\text{loop}} = \frac{\sqrt{l^2+\Delta y_R^2}}{4\pi l \Delta y_R} - \frac{\sqrt{l^2+\Delta y_L^2}}{4\pi l \Delta y_L}. \quad (70)$$

If we isolate the terms due to each of the two Δy coordinates:

$$w_{\Gamma,\text{loop}} = w_{\Gamma,\text{half}}(\Delta y_R) - w_{\Gamma,\text{half}}(\Delta y_L). \quad (71)$$

We can now substitute into the Duhamel integral to obtain the downwash at the specified offset for arbitrary changes in $\Gamma^j(t)$, summing over all such loops j to obtain the downwash at location i:

$$w^i_n(t) = -w^i_{2D}(t) + \sum_{j=0}^{N}\left(w_{\Gamma,\text{half}}(\tilde{t},\Delta y_R,c^j)\,\Gamma^j(0) + \int_0^{\tilde{t}(t)} w_{\Gamma,\text{half}}(\tilde{t}-\sigma,\Delta y_R,c^j)\frac{d\Gamma^j(\sigma)}{d\sigma}d\sigma\right) - \sum_{j=0}^{N}\left(w_{\Gamma,\text{half}}(\tilde{t},\Delta y_L,c^j)\,\Gamma^j(0) + \int_0^{\tilde{t}(t)} w_{\Gamma,\text{half}}(\tilde{t}-\sigma,\Delta y_L,c^j)\frac{d\Gamma^j(\sigma)}{d\sigma}d\sigma\right). \quad (72)$$

Note how similar to [20], we have to correct the determined downwash by subtracting the 2D wake $w^i_{2D}(t)$. Subracting $w^i_{2D}(t)$ is counter-intuitive, but can be elucidated by the following example. Referring back to Fig. 5, the downwash at point i is due the influence of all vortex loops j. If the wing were instead the special case of infinite span (and therefore circulation is constant over the span), all chordwise-oriented vorticity in the wake would cancel to zero, leaving only the influence $w^i_{2D}(t)$ of the starting vortex. However, the downwash from 3D effects $w^i_n(t)$ must be zero in this case to enforce $v^i_e = v^i_n$ as in standard blade element theory. As such, w^i_n must be carefully defined as *only* the downwash required to correct the blade element inlet velocity to include 3D effects.

Next, we make a separable assumption, namely that the downwash $w_{\Gamma,\text{half}}$ can be given as a product of two functions. One function is dependent on the travel distance $\tilde{t}$ (or vortex length $l(\tilde{t})$), and the other is dependent Δy:

$$w_{\Gamma,\text{half}}(\tilde{t},\Delta y,c) \approx \frac{2}{c}A_{w1}e^{b_{w1}\tilde{t}}C_1(\Delta y,c) + \frac{2}{c}A_{w2}e^{b_{w2}\tilde{t}}C_2(\Delta y,c) + \frac{1}{4\pi\Delta y}. \quad (73)$$

The constants $C_1(\Delta y,c)$ and $C_2(\Delta y,c)$, illustrated in Fig. 15b, are solved by least squares analysis to best match $w_{\Gamma,\text{half}}$ (Fig. 15c), and the term $1/(4\pi\Delta y)$ is the standard aerodynamic influence of an infinitely long horseshoe vortex leg. The inputs can be non-dimensionalized by the semichord to remove the chord length dependence of the result, allowing the utilization of a simple lookup table.

Finally, we can organize the constants C_1 and C_2 into a matrix equation, replace $1/(4\pi\Delta y)$ with the quasi-steady aerodynamic influence matrix W_n, and substitute the states $x^i_{w1}(t)$ and $x^i_{w2}(t)$ into the Duhamel integrals of Eq. (72):

$$\boldsymbol{w}_n(t) = W_n\boldsymbol{\Gamma}(t) + W_0\boldsymbol{\Gamma}(t) + W_1\boldsymbol{x}_{w1}(t) + W_2\boldsymbol{x}_{w2}(t), \quad (74)$$

where $\boldsymbol{w}_n(t)$ is the vector list of $w^i_n(t)$, $\boldsymbol{\Gamma}(t)$ of $\Gamma^i(t)$ etc. This downwash correction does not necessarily act exactly along the foil normal $\boldsymbol{n}$, but instead at a right angle to the oncoming flow $\boldsymbol{v}_\perp$ as the vortices are convected downstream, but the difference between those two components is a cosine error that is negligible for realistic angles of attack.

The three matrices of interest W_0, W_1, and W_2 are given element-by-element form as:

$$W_0^{ij} = -\delta_{ij}\frac{2}{c^i}[A_{w1} + A_{w2}] + \frac{2}{c^j}\left[A_{w1}C_1(\Delta y_R^{ij}, c^j) + A_{w2}C_2(\Delta y_R^{ij}, c^j)\right] - \frac{2}{c^j}\left[A_{w1}C_1(\Delta y_L^{ij}, c^j) + A_{w2}C_2(\Delta y_L^{ij}, c^j)\right], \quad (75)$$

$$W_1^{ij} = C_1(\Delta y_R^{ij}, c^j) - C_1(\Delta y_L^{ij}, c^j) - \delta_{ij}, \quad (76)$$

$$W_2^{ij} = C_2(\Delta y_R^{ij}, c^j) - C_2(\Delta y_L^{ij}, c^j) - \delta_{ij}, \quad (77)$$

where δ_{ij} is the Kronecker delta.

In summary, the states $x_{w1}^i(t)$ and $x_{w2}^i(t)$ track the 2D downwash of each element on itself, and the matrix equation maps these states to the downwash at other elements. This process required only two approximations from the full unsteady lifting line: exponential decaying wake effect and separable equations in $\tilde{t}$ and Δy.

Acknowledgments

The authors wish to thank all the members of the Massachusetts Institute of Technology (MIT) Towing Tank Laboratory for their fruitful discussions on aerodynamics and control throughout the development of this work. Additionally, M. Drela and R. Tedrake provided feedback on state-space methods for flapping flight, and G. Bousquet and A. Gao helped edit this manuscript.

The authors further wish to acknowledge funding support from the Singapore-MIT Alliance for Research and Technology, within the Center for Environmental Sensing and Modeling program; and from the MIT Sea Grant Program (contract number NA10OAR410086). This research was also conducted with Government support under and awarded by DoD, Air Force Office of Scientific Research, National Defense Science and Engineering Graduate (NDSEG) Fellowship, 32 CFR 168a.

References

[1] Cory, R. E., *Supermaneuverable perching*, Ph.D. thesis, Massachusetts Institute of Technology, 2010.

[2] Izraelevitz, J. S. and Triantafyllou, M. S., "Adding in-line motion and model-based optimization offers exceptional force control authority in flapping foils," *Journal of Fluid Mechanics*, Vol. 742, March 2014, pp. 5–34. doi:10.1017/jfm.2014.7.

[3] Abdulrahim, M. and Lind, R., "Using avian morphology to enhance aircraft maneuverability," *AIAA Atmospheric Flight Mechanics Conference and Exhibit*, 2006, p. 6643. doi:10.2514/6.2006-6643.

[4] Pennycuick, C., "Modelling the flying bird," *Theoretical ecology series (ISSN 1875-306X)*, Vol. 5, 2008.

[5] Videler, J. J., *Avian flight*, Oxford University Press, 2006. doi:10.1093/acprof:oso/9780199299928.001.0001.

[6] Bellman, R. E., *Adaptive control processes: a guided tour*, Princeton university press, 1961.

[7] Karpel, M., "Design for active flutter suppression and gust alleviation using state-space aeroelastic modeling," *Journal of Aircraft*, Vol. 19, No. 3, 1982, pp. 221–227. doi:10.2514/3.57379.

[8] Lucia, D. J., Beran, P. S., and Silva, W. A., "Reduced-order modeling: new approaches for computational physics," *Progress in Aerospace Sciences*, Vol. 40, No. 1, 2004, pp. 51–117. doi:10.1016/j.paerosci.2003.12.001.

[9] Lomax, H., Heaslet, M. A., Fuller, F. B., and Sluder, L., "Two-and three-dimensional unsteady lift problems in high-speed flight," *NACA-TR-1077*, 1952.

[10] Reissner, E. and Stevens, J. E., "Effect of finite span on the airload distributions for oscillating wings. II-methods of calculation and examples of application," *NACA-TN-1195*, 1947.

[11] Ansari, S., Żbikowski, R., and Knowles, K., "Aerodynamic modelling of insect-like flapping flight for micro air vehicles," *Progress in Aerospace Sciences*, Vol. 42, No. 2, 2006, pp. 129–172.

[12] Tobalske, B. and Dial, K., "Flight kinematics of black-billed magpies and pigeons over a wide range of speeds," *Journal of Experimental Biology*, Vol. 199, No. 2, 1996, pp. 263–280.

[13] Anderson, J., Streitlien, K., Barrett, D., and Triantafyllou, M., "Oscillating foils of high propulsive efficiency," *Journal of Fluid Mechanics*, Vol. 360, April 1998, pp. 41–72. doi:10.1017/S0022112097008392.

[14] Dickinson, M. H. and Gotz, K. G., "Unsteady aerodynamic performance of model wings at low Reynolds numbers," *Journal of Experimental Biology*, Vol. 174, No. 1, 1993, pp. 45–64.

[15] Birch, J. M. and Dickinson, M. H., "Spanwise flow and the attachment of the leading-edge vortex on insect wings," *Nature*, Vol. 412, No. 6848, 2001, pp. 729–733. doi:10.1038/35089071.

[16] Eldredge, J. D. and Darakananda, D., "Reduced-Order Two-and Three-Dimensional Vortex Modeling of Unsteady Separated Flows," *53rd AIAA Aerospace Sciences Meeting*, 2015, p. 1749.

[17] Leishman, J. and Beddoes, T., "A Semi-Empirical Model for Dynamic Stall," *Journal of the American Helicopter Society*, Vol. 34, No. 3, 1989, pp. 3–17. doi:10.4050/JAHS.34.3.

[18] Taha, H. E., Hajj, M. R., and Beran, P. S., "State-space representation of the unsteady aerodynamics of flapping flight," *Aerospace Science and Technology*, Vol. 34, February 2014, pp. 1–11.

[19] Peters, D. A. and He, C. J., "Finite state induced flow models. II-Three-dimensional rotor disk," *Journal of Aircraft*, Vol. 32, No. 2, 1995, pp. 323–333.

[20] Jones, R. T., "The unsteady lift of a wing of finite aspect ratio," *NACA-TR-681*, 1940.

[21] Ahmadi, A. R. and Widnall, S. E., "Unsteady lifting-line theory as a singular perturbation problem," *Journal of Fluid Mechanics*, Vol. 153, April 1985, pp. 59–81.

[22] Wilmott, P., "Unsteady lifting-line theory by the method of matched asymptotic expansions," *Journal of fluid mechanics*, Vol. 186, January 1988, pp. 303–320.

[23] Zhu, Q., Wolfgang, M., Yue, D., and Triantafyllou, M., "Three-dimensional flow structures and vorticity control in fish-like swimming," *Journal of Fluid Mechanics*, Vol. 468, October 2002, pp. 1–28. doi:10.1017/S002211200200143X.

[24] Scherer, J. O., "Experimental and theoretical investigation of large amplitude oscillation foil propulsion systems," Tech. Rep. TR-662-1-F, DTIC Document, 1968.

[25] Lan, C. E., "A quasi-vortex-lattice method in thin wing theory," *Journal of Aircraft*, Vol. 11, No. 9, 1974, pp. 518–527. doi:10.2514/3.60381.

[26] Vest, M. S. and Katz, J., "Unsteady aerodynamic model of flapping wings," *AIAA journal*, Vol. 34, No. 7, 1996, pp. 1435–1440.

[27] Long, L. N. and Fritz, T. E., "Object-oriented unsteady vortex lattice method for flapping flight," *Journal of Aircraft*, Vol. 41, No. 6, 2004, pp. 1275–1290.

[28] Stanford, B. K. and Beran, P. S., "Analytical sensitivity analysis of an unsteady vortex-lattice method for flapping-wing optimization," *Journal of Aircraft*, Vol. 47, No. 2, 2010, pp. 647–662.

[29] Katz, J. and Plotkin, A., *Low-speed aerodynamics*, Vol. 13, Cambridge University Press, Cambridge UK, 2001.

[30] Phillips, W. and Snyder, D., "Modern adaptation of Prandtl's classic lifting-line theory," *Journal of Aircraft*, Vol. 37, No. 4, 2000, pp. 662–670. doi:10.2514/2.2649.

[31] Hoerner, S. F. and Borst, H. V., *Fluid-dynamic lift: practical information on aerodynamic and hydrodynamic lift*, Hoerner Fluid Dynamics Brick Town, NJ, 1985.

[32] Drela, M., "ASWING 5.81 Technical Description - Unsteady Extension," 2008.

[33] Theodorsen, T., "General theory of aerodynamic instability and the mechanism of flutter," *NACA-TR-496*, 1949.

[34] Weissinger, J., "The lift distribution of swept-back wings," *NACA-TM-1120*, 1947.

[35] Prandtl, L., "Tragflügeltheorie. I. Mitteilung," *Nachrichten von der Gesellschaft der Wissenschaften zu Göttingen, Mathematisch-Physikalische Klasse*, Vol. 1918, December 1918, pp. 451–477.

[36] Wagner, H., "Über die Entstehung des dynamischen Auftriebes von Tragflügeln," *ZAMM-Journal of Applied Mathematics and Mechanics/Zeitschrift für Angewandte Mathematik und Mechanik*, Vol. 5, No. 1, 1925, pp. 17–35.

[37] Karman, T. V., "Airfoil Theory for Non-Uniform Motion," *Journal of the Aeronautical Sciences*, Vol. 5, No. 10, Aug. 1938, pp. 379–390. doi:10.2514/8.674.

[38] Brunton, S. L. and Rowley, C. W., "Empirical state-space representations for Theodorsen's lift model," *Journal of Fluids and Structures*, Vol. 38, January 2013, pp. 174–186. doi:10.1016/j.jfluidstructs.2012.10.005.

[39] Bergami, L., Gaunaa, M., and Heinz, J., "Indicial lift response function: an empirical relation for finite-thickness airfoils, and effects on aeroelastic simulations," *Wind Energy*, Vol. 16, No. 5, 2013, pp. 681–693. doi:10.1002/we.1516.

[40] Berci, M., "Lift-Deficiency Functions of Elliptical Wings in Incompressible Potential Flow: Jones Theory Revisited," *Journal of Aircraft*, 2015, pp. 1–4. doi:10.2514/1.C033515.

[41] Hansen, M. H., Gaunaa, M., and Aagaard Madsen, H., "A Beddoes-Leishman type dynamic stall model in state-space and indicial formulations," *Risø-R-1354 (EN), Risø National Laboratory*, June 2004.

[42] Dickinson, M., "The effects of wing rotation on unsteady aerodynamic performance at low Reynolds numbers," *Journal of experimental biology*, Vol. 192, No. 1, 1994, pp. 179–206.

[43] Glauert, H., *The elements of aerofoil and airscrew theory*, Cambridge University Press, 1926.

[44] Fossen, T. I. and Fjellstad, O.-E., "Nonlinear modelling of marine vehicles in 6 degrees of freedom," *Mathematical Modelling of Systems*, Vol. 1, No. 1, 1995, pp. 17–27. doi:10.1080/13873959508837004.

[45] Newman, J. N., *Marine hydrodynamics*, MIT press, 1977.

[46] Munk, M. M., "Fluid mechanics, part II," *Aerodynamic Theory*, Springer, 1934, pp. 224–304.

[47] Tedrake, R., "Drake: A planning, control, and analysis toolbox for nonlinear dynamical systems," 2014.

[48] Nise, N. S., *Control Systems Engineering*, John Wiley & Sons, 2007.

[49] Triantafyllou, M., Triantafyllou, G., and Gopalkrishnan, R., "Wake mechanics for thrust generation in oscillating foils," *Phys. Fluids A*, Vol. 3, No. 12, 1991, pp. 2835–2837. doi:10.1063/1.858173.

[50] Taylor, G. K., Nudds, R. L., and Thomas, A. L., "Flying and swimming animals cruise at a Strouhal number tuned for high power efficiency," *Nature*, Vol. 425, No. 6959, 2003, pp. 707–711. doi:10.1038/nature02000.

[51] Izraelevitz, J. S. and Triantafyllou, M. S., "A novel degree of freedom in flapping wings shows promise for a dual aerial/aquatic vehicle propulsor," *2015 IEEE International Conference on Robotics and Automation (ICRA)*, IEEE, 2015, pp. 5830–5837.

[52] Nudds, R. L., Taylor, G. K., and Thomas, A. L., "Tuning of Strouhal number for high propulsive efficiency accurately predicts how wingbeat frequency and stroke amplitude relate and scale with size and flight speed in birds," *Proceedings of the Royal Society of London. Series B: Biological Sciences*, Vol. 271, No. 1552, 2004, pp. 2071–2076.

[53] Garrick, I., "On some reciprocal relations in the theory of nonstationary flows," *NACA-TR-629*, 1938.